J. Fluid Mech. (1994), *vol.* 261, *pp.* 169–198

Free-surface Taylor vortices

By F. J. WANG[1]† AND G. A. DOMOTO[2]

[1] Department of Mechanical Engineering, Columbia University, New York, NY 10027, USA

[2] Xerox Corporation, Webster Research Center, Mechanical Engineering Science Laboratory, 141 Webber Avenue, North Tarrytown, NY 10591, USA

(Received 9 January 1992 and in revised form 13 August 1993)

The hydrodynamic instability of a viscous incompressible flow with a free surface is studied both numerically and experimentally. While the free-surface flow is basically two-dimensional at low Reynolds numbers, a three-dimensional secondary flow pattern similar to the Taylor vorticies between two concentric cylinders appears at higher rotational speeds. The secondary flow has periodic velocity components in the axial direction and is characterized by a distinct spatially periodic variation in surface height similar to a standing wave. A numerical method, using boundary-fitted coordinates and multigrid methods to solve the Navier–Stokes equations in primitive variables, is developed to treat two-dimensional free-surface flows. A similar numerical technique is applied to the linearized three-dimensional perturbation equations to treat the onset of secondary flows. Experimental measurements have been obtained using light sheet techniques to visualize the secondary flow near the free surface. Photographs of streak lines were taken and compared to the numerical calculations. It has been shown that the solution of the linearized equations contains most of the important features of the nonlinear secondary flows at Reynolds number higher than the critical value. The experimental results also show that the numerical method predicts well the onset of instability in terms of the critical wavenumber and Reynolds number.

1. Introduction

Free-surface problems, sometimes referred to as moving boundary problems, have long received academic attention and industrial interest. The free-surface can be an interface between two fluids with difference in density, or an interface between solid and liquid in the process of melting or solidification, etc. Free-surface problems encompass a wide range of engineering interest and application, including two-phase flows, coating and crystal growth processes, lubrication of bearings, electrochemical machining, and free-surface waves in viscous flows.

The free-surface problem can be mathematically modelled as an initial boundary value problem. However, unlike prescribed domain problems, the main difficulty in solving the free-surface problem arises from the fact that the free-surface location and shape must be included as unknowns in the solution procedure. From the hydrodynamic point of view, a complete formulation of the moving free surface involves the proper handling of two important effects: the surface tension and the viscous stress in both the tangential and normal directions on the free surface. Both effects involve the calculation of the orientation and shape of the free surfaces.

† Present address: Xerox Corporation, Webster Research Center, Marking Physics Laboratory, 800 Phillips Road, 0114-23D, Webster, NY 14580, USA.

Furthermore, free-surface flows can often be hydrodynamically and thermally unstable. Well known examples include the Rayleigh–Bénard (thermal) instability in a horizontal layer of fluid heated from below, and the Kelvin–Helmholtz (hydrodynamic) instability in a heterogeneous fluid in which different layers are in relative motion. The principle of the exchange of stabilities (Chandrasekhar 1981) is valid for these two instabilities as well as for some Taylor–Couette flows (Taylor 1923). That is, at the onset of instability the two-dimensional flow field perturbed by small disturbances will evolve into three-dimensional stationary motions different from the original steady state. These stationary flows have fixed mode shape and are time independent (no periodic motion in time). To make the analysis of any two-dimensional free-surface flow complete, the three-dimensional flow instability must be considered.

In this paper we shall present both a numerical calculation and experimental results. We have performed flow visualization by streak photography, as well as other measurements, of a two-dimensional viscous incompressible free-surface flow. It is driven by an immersed rotating cylinder in a long rectangular trough. This study includes the solution of two-dimensional steady-state flows (the basic flows) and the calculation of the onset of the secondary flows. At sufficiently high Reynolds number the secondary flows gives rise to distinct motion in the axial direction similar to Taylor vorticies. A special feature of these secondary flows is the periodic spatial variation of free-surface shape similar to a standing wave in the axial direction. We call these secondary flows *free-surface Taylor vortex flows.*

To calculate the basic flows, we devise a general finite-difference algorithm. Using boundary-fitted coordinates, the full Navier–Stokes equations and the Poisson equation for pressure are discretized on a non-staggered grid. The computation is therefore performed on the fixed square grid regardless of the shape and the movement of the physical boundaries. The primitive variables, velocities and pressure, are computed in a time marching scheme. The shapes of the surfaces are updated from their initial geometries by the kinematic condition at each time step. Along with the change of shape, the computational meshes are redistributed by solving a set of elliptic equations (Thompson, Warsi & Mastin 1982, 1985). Multigrid methods are employed for both the fluid and grid equations for better numerical efficiency. For the three-dimensional flows, linear stability analysis is performed subject to homogeneous boundary conditions. The advantage of linear stability analysis is that it is carried out in the two-dimensional domain. Linear stability analysis predicts the critical parameters as well as the disturbed flow fields for the onset of three-dimensional instabilities. Unlike the conventional approaches (Taylor 1923; Chandrasekhar 1981; Ruschak 1981; Coyle 1984, etc.) to treat the linear system as an eigenvalue problem, we do not pursue the eigenvalue directly. Instead, we treat it as an initial value problem and apply a method similar to that used for calculating the basic flow to solve for the disturbances. The eigenvalues can be obtained when the neutral stability points are numerically determined. To simulate the secondary flows, at least near the neutral stability point, the flow fields are numerically constructed by superimposing the disturbances (the solutions of the linearized Navier–Stokes equations of disturbances) onto the basic flows. The secondary flows are then approximated and visualized by numerically computed trajectories.

The numerical results are verified experimentally. Free-surface shapes can be easily measured and compared with the calculations. Also, the critical parameters, i.e. the critical Reynolds number, Re_{cr}, and the wavenumber, f_{cr}, are measured at the onset of the instability. Flow visualization has been performed using light sheet and streak photography techniques. The experimental fluid in use is a clear silicon-based oil, Dow

Corning 200 fluid. A 12 mW helium–neon laser is used as a concentrated light source to illuminate the suspended scattering particles, which are Kalliroscope flakes (Matisse & Gorman 1984). Photographs are taken for flows with Reynolds number in the range of 1.1 Re_{cr} to 1.2 Re_{cr}.

The formulation of equations and numerical methods will only be summarized briefly. For a detailed description, see Wang (1990).

2. Mathematical modelling

2.1. *Grid generation*

The grid is numerically generated by a set of elliptic partial differential equations according to Thompson *et al.* (1985):

$$\alpha x_{\xi\xi} - 2\beta x_{\xi\eta} + \gamma x_{\eta\eta} = -J^2(Px_\xi + Qx_\eta),$$

$$\alpha y_{\xi\xi} - 2\beta y_{\xi\eta} + \gamma y_{\eta\eta} = -J^2(Py_\xi + Qy_\eta),$$

where $$\alpha = x_\eta^2 + y_\eta^2, \quad \beta = x_\xi x_\eta + y_\xi y_\eta, \quad \gamma = x_\xi^2 + y_\xi^2, \quad J = x_\xi y_\eta - x_\eta y_\xi, \tag{2.1}$$

with the forcing functions of P and Q to control the grid spacing. They are

$$\begin{aligned} P(\xi,\eta) &= -\sum a_i \operatorname{sgn}(\xi-\xi_i)\exp\{-c_i|\xi-\xi_i|\} \\ &\quad -\sum b_j \operatorname{sgn}(\xi-\xi_j)\exp\{-d_j[(\xi-\xi_i)^2+(\eta-\eta_j)^2]^{\frac{1}{2}}\}, \\ Q(\xi,\eta) &= -\sum e_i \operatorname{sgn}(\eta-\eta_i)\exp\{-f_i|\eta-\eta_i|\} \\ &\quad -\sum g_j \operatorname{sgn}(\eta-\eta_j)\exp\{-h_j[(\xi-\xi_i)^2+(\eta-\eta_j)^2]^{\frac{1}{2}}\}; \end{aligned}$$

a_i and c_i control the extent of attraction of the ξ-line toward the ξ_i-line, while b_j and d_j control the extent of attraction of the ξ-line toward the point (ξ_j, η_j), and the effect of e_i, f_i, g_j and h_j on η-lines is similar.

The elliptic grid generation scheme was chosen because of its flexibility in providing adaptive grid control, which is essential in treating the free surface. Some multigrid routines have been developed to treat elliptic equations very efficiently (Hackbusch & Trottenberg 1981).

2.2. *Governing equations and boundary conditions of the basic flows*

A two-dimensional Newtonian incompressible fluid with homogeneous material properties under a gravity field can be modelled by the following non-dimensional continuity and Navier–Stokes equations (u_1 and v_1 represent the velocity components in the Cartesian coordinates, p_1 is the pressure):

$$\frac{\partial u_1}{\partial x} + \frac{\partial v_1}{\partial y} = 0,$$

$$\frac{\mathrm{D}u_1}{\mathrm{D}t} = -p_{1_x} + \frac{1}{Re}\nabla^2 u_1, \tag{2.2}$$

$$\frac{\mathrm{D}v_1}{\mathrm{D}t} = -p_{1_y} + \frac{1}{Re}\nabla^2 v_1 - \frac{1}{Fd}. \tag{2.3}$$

The pressure equation can be derived from the divergence of the momentum equations, where the viscous term vanishes due to the incompressibility condition:

$$\nabla^2 p_1 = -\left(\frac{\partial}{\partial x}\frac{\mathrm{D}u_1}{\mathrm{D}t} + \frac{\partial}{\partial y}\frac{\mathrm{D}v_1}{\mathrm{D}t}\right). \tag{2.4}$$

The governing parameters Re (Reynolds number), Fd (Froude number) are (where ρ, μ, g, U_0, L_0 are density, viscosity, gravity, characteristic velocity and length respectively:

$$Re = \frac{\rho U_0 L_0}{\mu}, \quad Fd = \frac{U_0^2}{gL_0}.$$

The boundary conditions for the pressure equation (2.4) are:

(i) on the rigid surface, the pressure gradients, obtained directly from the Navier–Stokes equations, are specified:

$$\frac{\partial P_1}{\partial x} = -\frac{\mathrm{D}u_1}{\mathrm{D}t} - \frac{1}{Re}\frac{\partial \omega_1}{\partial y}, \quad \frac{\partial P_1}{\partial y} = -\frac{\mathrm{D}v_1}{\mathrm{D}t} + \frac{1}{Re}\frac{\partial \omega_1}{\partial x}, \tag{2.5a,b}$$

where the vorticity ω is

$$\omega_1 = \frac{\partial v_1}{\partial x} - \frac{\partial u_1}{\partial y};$$

(ii) on the free surface, the normal stress condition is applied; that is (neglecting the viscous stress of air because of its low viscosity) using the Einstein summation notation where repeated subscripts are summed,

$$p_1 = P_{atm} + \frac{1}{Re} n_i n_j T_{ij} + We\left(\frac{1}{R_s}\right), \tag{2.5c}$$

where the Webber number, We, and the radius of curvature, R_s, are given by

$$We = \frac{\sigma}{\rho U_0^2 L_0}, \quad R_s = \frac{(1+y_x^2)^{1.5}}{y_{xx}}.$$

P_{atm}, σ and T_{ij} are the atmospheric pressure, the coefficient of surface tension and the viscous stress tensor; n_i represent the unit vectors in the direction normal to the free surface.

For the momentum equations (2.2)–(2.3), the boundary conditions are:

(i) no slip on the rigid surface, i.e.

$$u_1 = u_{surface}, \quad v_1 = v_{surface}; \tag{2.6a}$$

(ii) No shear stress on the free surface, which is the tangential stress condition (again, neglecting the viscous stress of air):

$$t_i n_j T_{ij} = 0. \tag{2.6b}$$

Here t_i is the unit vector in the direction tangent to the free surface. Since (2.2)–(2.3) are elliptic equations, one more boundary condition is required. In this work, the continuity equation is enforced as Neumann-type boundary condition on free surfaces:

$$\frac{\partial u_1}{\partial x} + \frac{\partial v_1}{\partial y} = 0 \tag{2.6c}$$

2.3. *Secondary flows – linear stability analysis*

Perturb the basic flow with an infinitesimal disturbance (u', v', w', p', h'), and let the perturbed state be given as

$$U = u_1 + u' = u_1 + u(x, y, t)\,e^{-ifz}, \tag{2.7a}$$

$$V = v_1 + v' = v_1 + v(x, y, t)\,e^{-ifz}, \tag{2.7b}$$

$$W = w' = w(x, y, t)\,e^{-ifz}, \tag{2.7c}$$

$$P = p_1 + p' = p_1 + p(x, y, t)\,e^{-ifz}, \tag{2.7d}$$

$$H = h_1 + h' = h_1 + h(x, y, t)\,e^{-ifz}, \tag{2.7e}$$

where h_1 is the free surface height of the basic flow and f is the non-dimensional wavenumber ($2\pi L_0$/wavelength). Substitute (2.7) into (2.2)–(2.4), and linearize the equations for a small disturbance; then

$$\frac{\partial u}{\partial x} + \frac{\partial v}{\partial y} - ifw = 0, \tag{2.8a}$$

$$\frac{Du}{Dt} = -\frac{\partial p}{\partial x} + \frac{1}{Re}(\nabla^2 u - f^2 u) - u\frac{\partial u_1}{\partial x} - v\frac{\partial u_1}{\partial y}, \tag{2.8b}$$

$$\frac{Dv}{Dt} = -\frac{\partial p}{\partial y} + \frac{1}{Re} + \frac{1}{Re}(\nabla^2 v - f^2 v) - u\frac{\partial v_1}{\partial x} - v\frac{\partial v_1}{\partial y}, \tag{2.8c}$$

$$\frac{Dw}{Dt} = ifp + \frac{1}{Re}(\nabla^2 w - f^2 w), \tag{2.8d}$$

where

$$\frac{D}{Dt} = \frac{\partial}{\partial t} + u_1\frac{\partial}{\partial x} + v_1\frac{\partial}{\partial y}, \quad \nabla^2 = \frac{\partial^2}{\partial x^2} + \frac{\partial^2}{\partial y^2}. \tag{2.8e}$$

The corresponding boundary conditions can be derived by perturbing (2.5)–(2.6). All the governing equations and boundary conditions for the basic flows and the perturbations are transformed into boundary-fitted coordinates as shown below.

2.4. *Transformation*

Transforming the fluid governing equations and boundary conditions to the (ξ, η)-plane yields the following system of equations:

(i) *The basic flows* (u_1, v_1, $\mathscr{P}_1$, h_1) *where* ($\mathscr{P}_1 = p_1 + y/Fd$)

The momentum equations are

$$\frac{Du_1}{Dt} = -\frac{1}{J}[(y_\eta \mathscr{P}_1)_\xi - (y_\xi \mathscr{P}_1)_\eta] + \frac{1}{Re}\nabla^2 u_1, \tag{2.9a}$$

$$\frac{Dv_1}{Dt} = -\frac{1}{J}[(x_\xi \mathscr{P}_1)_\eta - (x_\eta \mathscr{P}_1)_\xi] + \frac{1}{Re}\nabla^2 v_1, \tag{2.9b}$$

with boundary conditions:
on the rigid surface

$$u_1 = u_{surface}, \quad v_1 = v_{surface}; \tag{2.9c}$$

on the free surface (t_x, t_y, n_x, and n_y represent the Cartesian components of the tangential and normal unit vectors of the free surface)

$$(y_\eta u_1 - x_\eta v_1)_\xi + (x_\xi v_1 - y_\xi u_1)_\eta = 0, \tag{2.9d}$$

$$2t_x n_x \frac{\partial u_1}{\partial t} + (t_x n_y + t_y n_x)\left(\frac{\partial u_1}{\partial y} + \frac{\partial v_1}{\partial x}\right) + 2y_y n_y \frac{\partial v_1}{\partial y} = 0. \tag{2.9e}$$

The pressure equation is

$$J\nabla^2\mathscr{P}_1 = \left(x_\eta \frac{\mathrm{D}v_1}{\mathrm{D}t} - y_\eta \frac{\mathrm{D}u_1}{\mathrm{D}t}\right)_\xi + \left(-x_\xi \frac{\mathrm{D}v_1}{\mathrm{D}t} + y_\xi \frac{\mathrm{D}u_1}{\mathrm{D}t}\right)_\eta \tag{2.10a}$$

with boundary conditions:
on the rigid surface

$$\left(\alpha^{\frac{1}{2}} \frac{\partial \mathscr{P}_1}{\partial n}\right)_{(\xi)} = x_\eta \frac{\mathrm{D}v_1}{\mathrm{d}t} - y_\eta \frac{\mathrm{D}u_1}{\mathrm{d}t} - \frac{1}{Re}\frac{\partial \omega_1}{\partial \eta} \quad \text{along } \xi = \text{constant}, \tag{2.10b}$$

$$\left[\gamma^{\frac{1}{2}} \frac{\partial \mathscr{P}_1}{\partial n}\right]_{(\eta)} = y_\xi \frac{\mathrm{D}u_1}{\mathrm{d}t} - x_\xi \frac{\mathrm{D}v_1}{\mathrm{d}t} + \frac{1}{Re}\frac{\partial \omega_1}{\partial \xi} \quad \text{along } \eta = \text{constant}; \tag{2.10c}$$

on the free surface

$$\mathscr{P}_1 = P_{atm} + \frac{2}{Re}\left\{n_x^2 \frac{\partial u_1}{\partial x} + n_x n_y\left(\frac{\partial u_1}{\partial y} + \frac{\partial v_1}{\partial x}\right) + n_y^2 \frac{\partial v_1}{\partial y}\right\} + We\left(\frac{1}{R_s}\right) + \frac{y}{Fd}, \tag{2.10d}$$

where the vorticity, ω_1, and the curvature of the free surface, R_s, are

$$\omega_1 = \frac{\partial v_1}{\partial x} - \frac{\partial u_1}{\partial y}, \quad \frac{1}{R_s} = \frac{y_\xi x_{\xi\xi} - x_\xi y_{\xi\xi}}{(x_\xi^2 + x_\xi^2)^{1.5}}. \tag{2.10e}$$

Finally, the height of the free surface, $h_1 = y(x, t)$ can be determined from the kinematic condition applied on the free surface,

$$\frac{\partial h_1}{\partial t} = v_1 - u_1 \frac{\partial h_1}{\partial x} \tag{2.11}$$

(ii) *The disturbances* (u, v, w, p, h)

The disturbance of the surface shape can be determined by perturbing the kinematic condition, (2.10)–(2.11). Therefore,

$$\frac{\partial h}{\partial t} = v - u\frac{\partial h_1}{\partial x} - u_1 \frac{\partial h}{\partial x}. \tag{2.12}$$

In (2.8), replace the disturbance w by iw. Therefore, a 90° phase difference, between the velocity disturbance in the z-direction and the other disturbances, is introduced. The system becomes

$$\frac{\mathrm{D}u}{\mathrm{D}t} = -\frac{\partial p}{\partial x} + \frac{1}{Re}(\nabla^2 u - f^2 u) - u\frac{\partial u_1}{\partial x} - v\frac{\partial u_1}{\partial y}, \tag{2.13a}$$

$$\frac{\mathrm{D}v}{\mathrm{D}t} = -\frac{\partial p}{\partial y} + \frac{1}{Re}(\nabla^2 v - f^2 v) - u\frac{\partial v_1}{\partial x} - v\frac{\partial v_1}{\partial y}, \tag{2.13b}$$

$$\frac{\mathrm{D}w}{\mathrm{D}t} = fp + \frac{1}{Re}(\nabla^2 w - f^2 w). \tag{2.13c}$$

The velocity disturbances are governed by the above equations with boundary conditions as follows:
on a rigid surface they are homogeneous boundary conditions:

$$u = v = w = 0; \tag{2.13d}$$

on a free surface

$$w = \frac{-1}{f}\left(\frac{\partial u}{\partial x}+\frac{\partial v}{\partial y}\right), \tag{2.13e}$$

$$2t_x t_y\left(\frac{\partial v}{\partial y}-\frac{\partial u}{\partial x}\right)+(t_x^2-t_y^2)\left(\frac{\partial u}{\partial y}+\frac{\partial v}{\partial x}\right) = -h\frac{\partial\left\{2t_x t_y\left(\frac{\partial v_1}{\partial y}-\frac{\partial u_1}{\partial x}\right)+(t_x^2-t_y^2)\left(\frac{\partial u_1}{\partial y}+\frac{\partial u_1}{\partial x}\right)\right\}}{\partial y}, \tag{2.13f}$$

$$t_x v - t_y u = \frac{1}{f}\left(t_x\frac{\partial w}{\partial y}-t_y\frac{\partial w}{\partial x}\right)+h\left(t_y\frac{\partial u_1}{\partial y}-t_x\frac{\partial v_1}{\partial y}\right), \tag{2.13g}$$

where t_x and $_y$ are the Cartesian components of unit tangential vector, t_i.

The pressure disturbance is determined by

$$\nabla^2 p - f^2 p = -\left\{\frac{\mathrm{D}\tilde{D}}{\mathrm{D}t}+2\frac{\partial}{\partial x}\left(u\frac{\partial u_1}{\partial x}+v\frac{\partial u_1}{\partial y}\right)+2\frac{\partial}{\partial y}\left(u\frac{\partial v_1}{\partial x}+v\frac{\partial v_1}{\partial y}\right)\right\}, \tag{2.14a}$$

where

$$\tilde{D} = \frac{\partial u}{\partial x}+\frac{\partial v}{\partial y}+fw,$$

with boundary conditions (in this study the free surface is taken to be on a constant η line):

on the free surface

$$p_{(\eta)} = -\frac{\partial P_1}{\partial y}h+\frac{2}{Re}\left(A+h\frac{\partial B}{\partial y}\right)+(We)k, \tag{2.14b}$$

where

$$A = t_y^2\frac{\partial u}{\partial x}-t_x t_y\left(\frac{\partial u}{\partial y}+\frac{\partial v}{\partial x}\right)+t_x^2\frac{\partial v}{\partial y},$$

$$B = t_y^2\frac{\partial u_1}{\partial x}-t_x t_y\left(\frac{\partial u_1}{\partial y}+\frac{\partial v_1}{\partial x}\right)+t_x^2\frac{\partial v_1}{\partial y},$$

$$k = \frac{1}{Rs}\left(\frac{x_{\xi\xi}h_\xi h_{\xi\xi}x_\xi+(x_\xi^2+y_\xi^2)f^2x_\xi h}{x_{\xi\xi}y_\xi-y_{\xi\xi}x_\xi}-\frac{3y_\xi h_\xi}{x_\xi^2+y_\xi^2}\right);$$

on the rigid surface

$$\left(\alpha^{\frac{1}{2}}\frac{\partial p}{\partial n}\right)_{(\xi)} = x_\eta\left(\frac{\mathrm{D}v}{\mathrm{D}t}+u\frac{\partial u_1}{\partial x}+v\frac{\partial u_1}{\partial y}\right)-y_\eta\left(\frac{\mathrm{D}v}{\mathrm{D}t}+u\frac{\partial v_1}{\partial x}+v\frac{\partial v_1}{\partial y}\right) -\frac{1}{Re}\left\{\frac{\partial\Omega}{\partial\eta}+f^2(x_\eta v-y_\eta u)-f\alpha^{\frac{1}{2}}\frac{\partial w}{\partial n}\right\}, \tag{2.14c}$$

$$\left(\gamma^{\frac{1}{2}}\frac{\partial p}{\partial n}\right)_{(\eta)} = y_\xi\left(\frac{\mathrm{D}u}{\mathrm{D}t}+u\frac{\partial u_1}{\partial x}+v\frac{\partial u_1}{\partial y}\right)-x_\xi\left(\frac{\mathrm{D}v}{\mathrm{D}t}+u\frac{\partial v_1}{\partial x}+v\frac{\partial v_1}{\partial y}\right) +\frac{1}{Re}\left\{\frac{\partial\Omega}{\partial\xi}+f^2(y_\xi u-x_\xi v)-f\gamma^{\frac{1}{2}}\frac{\partial w}{\partial n}\right\}, \tag{2.14d}$$

where $$\Omega = \frac{\partial v}{\partial x} - \frac{\partial u}{\partial y}$$

It should be noted that the Laplacian operator, ∇^2, and the total time derivative, $\mathrm{D}/\mathrm{D}t$, in (2.8e) are two-dimensional. Therefore, the $\mathrm{D}/\mathrm{D}t$ in (2.12)–(2.14) are taken along the same characteristics as the basic flow.

3. Numerical schemes

A finite-difference method, with truncation error of second order in space and first order in time, was developed for the solution of the system defined in (2.9)–(2.14). It can be characterized as follows:

(i) The unknown primitive variables, (u_1, v_1, p_1, h_1), for two-dimensional basic flows and their corresponding three-dimensional disturbances, (u', v', w', p', h'), are computed on a non-staggered grid with specified initial conditions in a time-marching process.

(ii) This is an implicit scheme except that the shape of the free surface is updated explicitly. That is, all the other difference approximations and function values, for both the governing equations and boundary conditions, are evaluated implicitly at the most recent time level. The inertial terms are calculated by the Eulerian–Lagrangian method (Casulli 1986, 1987). It should be noted that since all the transformed equations are solved in the curvilinear coordinates (ξ, η), and the physical boundaries change before any steady state is reached, the curvilinear coordinate system itself is time varying. Therefore, applying the Eulerian–Lagrangian method to solve the basic flows in such systems requires extra treatment, which is described in Appendix A. Such treatment, however, is not required for the calculation of disturbances since these calculations are carried out on the fixed grid derived from the steady-state solution of the basic flow.

To be more specific about the numerical procedure, the following steps were applied. For the basic flow, after all the flow variables have converged from solving (2.9)–(2.10) iteratively at the present time level, the free surfaces are moved according to the kinematic condition, (2.11). Then the mesh is updated by solving (2.1) from the updated boundaries to complete the computational cycle for one time step. A similar procedure is followed to treat (2.12)–(2.14), except that two more parameters are calculated at each time step for the purpose of determination of the flow stability. They are

$$K = \sum(u^2 + v^2 + w^2), \quad G = \frac{K|_{\text{at time}=n+1}}{K|_{\text{at time}=n}}; \tag{3.1}$$

the summation is taken over the whole computational domain. They will be referred to as total *disturbance kinetic energy* (K) and *amplification factor* (G). If the flow system is unstable this will be reflected by the values of the disturbance kinetic energy, i.e. K grows without bound. Also, it has been observed in this study that the amplification factor grows or decays asymptotically in time towards constants, if the eigenvalues of the homogeneous system are real. If the asymptotic value of G is less than 1 the system is stable.

(iii) A conservation discretization of the differential equations was adopted. With the use of the conservative forms, the discretized pressure equation could satisfy its compatibility criterion automatically if a consistent procedure for discretization is followed. Failing to satisfy the compatibility criterion will result in difficulties in obtaining convergent solutions for the Poisson equation with Neumann boundary

Critical parameters	Previous studies (Sparrow *et al.* 1964; Walowit *et al.*1964)	Numerical results: Present method, Grid 1 (197×49)	Numerical results: Present method, Grid 2 (99×25)	Numerical results: Present method, Grid 3 (65×19)
Reynolds number (Re_{cr})	68.18–68.19	68.5	70.8	72.5
Wavenumber (f_{cr}) ($f = 2\pi R_1$/wavelength)	3.16	3.16	3.17	3.20

TABLE 1. Concentric cylinder flow ($R_2/R_1 = 2$)

conditions. A conventional remedy for this problem is to modify either the boundary conditions or the source terms of the pressure equation to fit the criterion (Biringen & Cook 1988; Ghia, Hankey & Hodge 1977). A preferred procedure, proposed by Abdallah (1987) for cavity flows in Cartesian coordinates, was implemented in the present method (see Appendix B). Abdallah pointed out that the compatibility condition is not satisfied mostly because of the inconsistency of discretization between the Poisson equation and its boundary conditions. This scheme is further extended for general curvilinear coordinates (Wang 1990) in conjunction with the utilization of Cartesian velocity components, the conservative transformation and the Eulerian–Lagrangian method. A similar approach has been developed by Mansour & Hamed (1990). They applied the scheme to orthogonal curvilinear systems using contravariant velocity components and an explicit difference scheme.

(iv) A corrective scheme by Hirt & Harlow (1967) for incompressibility is used. Since continuity is not enforced directly in the present numerical method, proper correction of pressure is the only method for assuring incompressibility. To ensure that the solution method minimizes dilation ($D = u_x + v_y$), the dilation at time $n+1$ is taken as zero in (2.10*a*). The stability analysis is treated in a similar fashion in (2.13*a*). By doing this, the deviation from incompressibility can be suppressed during the transient solution and is minimal when steady-state solutions are obtained.

(v) All the difference equations, including the grid equation, are solved by Gauss–Seidel iteration using a V-cycle full approximation scheme multigrid method (Hackbusch & Trottenberg 1992). We employed three levels of grid with mesh sizes $M \times N$, $2M \times 2N$ and $4M \times 4N$.

Test case: *Taylor vorticies in the annulus of two concentric cylinders*

To test the performance of our initial-value code in solving for two-dimensional basic flows and for three-dimensional disturbances, we first applied it to investigate the Taylor–Couette flows in the annulus of concentric cylinders with radii ratio (R_2/R_1) of 2:1. The flow is driven by the inner cylinder rotating at constant speed. The general numerical procedure of determining the onset of instabilities is discussed here using the Taylor–Couette flow as an example. We started the calculation on a coarse grid with node numbers in the circumferential and radial direction of 65 by 19 (grid 3, see table 2). For testing purposes, we did not assume axisymmetry in modelling for either the basic flows or the disturbances. Like the time-marching process used in calculating the two-dimensional basic flows, the three-dimensional disturbances were computed from their initial conditions. Hence, after the solutions of the basic flows are obtained, any

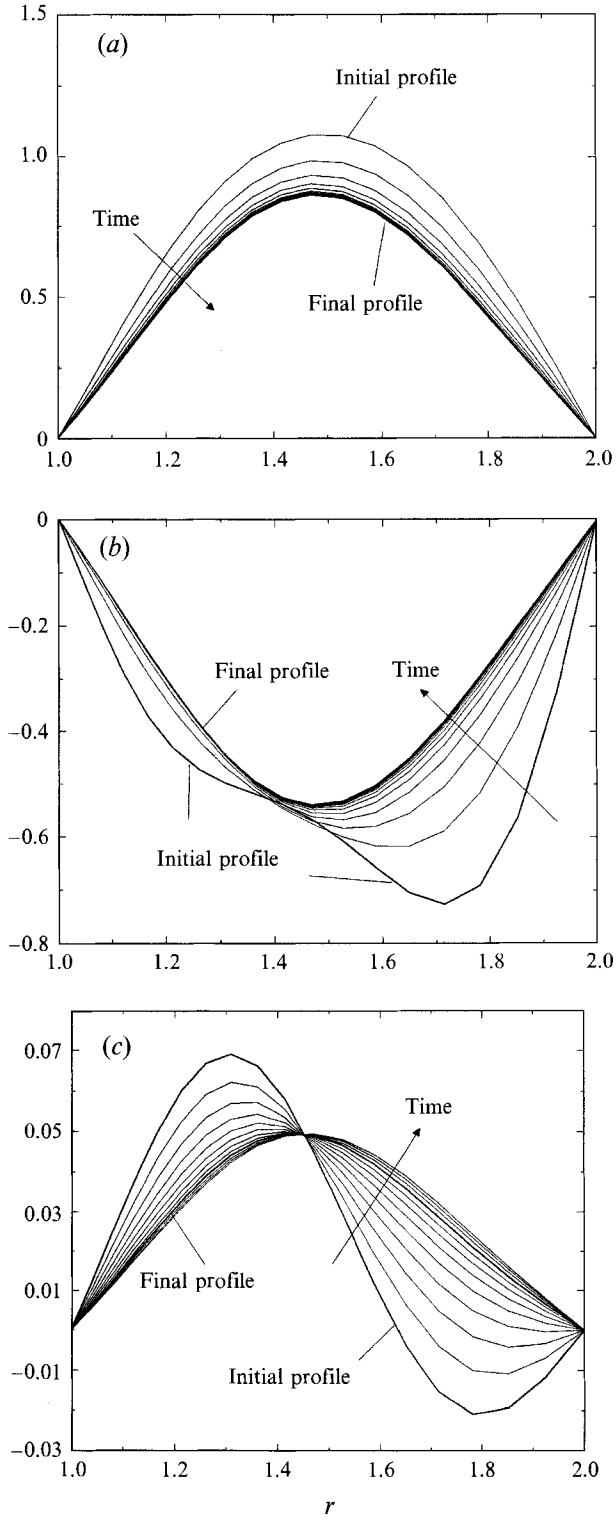

FIGURE 1. The evolution in time of velocity disturbance, U'_θ, corresponding to different initial conditions: (*a*) $U'_\theta = a(r^2+br+c)$, (*b*) $U'_\theta = a(r-R_1)(r-R_2)(r^2+br+c)$, (*c*) $U'_\theta = a\sin[2\pi(r-R_1)/(R_2-R_1)]$.

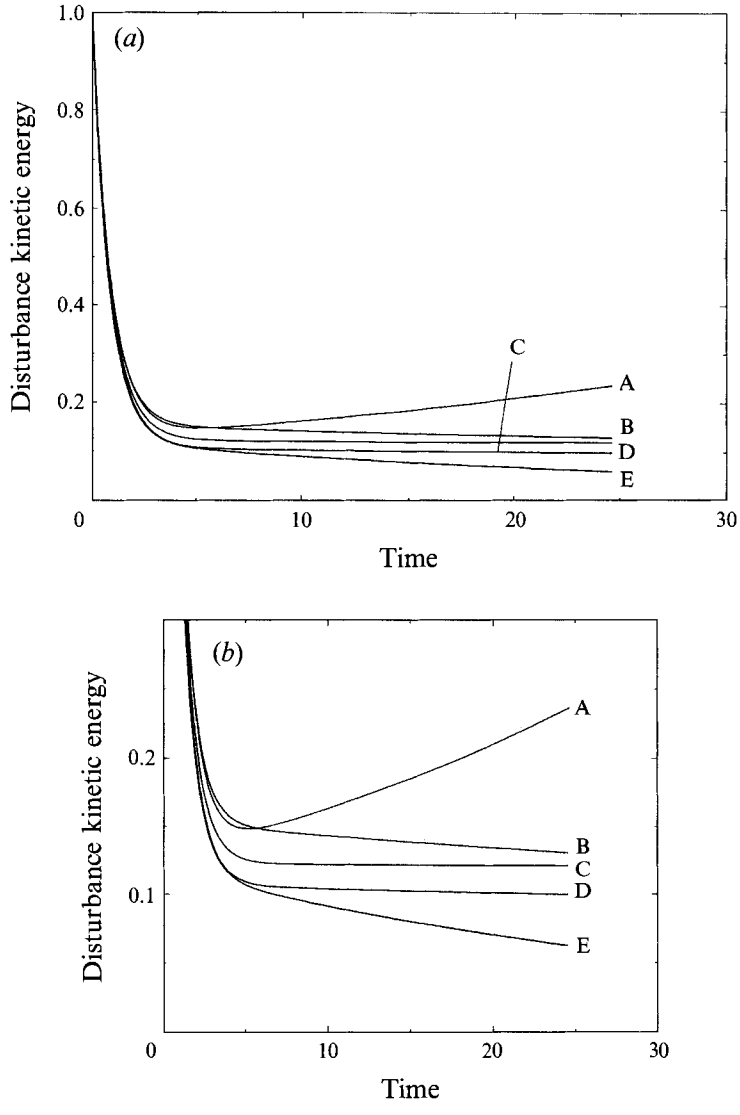

FIGURE 2. (*a*) Disturbance kinetic energy, (*b*) Enlargement. Curve A, $Re = 75.0$, wavenumber = 3.2; B, $Re = 72.5$, wavenumber 3.0; C, $Re = 72.5$, wavenumber = 3.2; D, $Re = 72.5$, wavenumber = 3.6; E, $Re = 70.0$, wavenumber = 3.2.

initial disturbance which satisfies the conservation of mass, namely, $\tilde{D} = 0$, can be used as an initial condition for the equations of perturbation. For example, let initial radial disturbances be zero; three different disturbances of circumferential velocity, U'_θ, with specific shape functions are chosen: (i) $U'_\theta = a(r^2 + br + c)$, (ii)

$$U'_\theta = a(r - R_1)(r - R_2)(r^2 + br + c),$$

and (iii) $U'_\theta = a \sin[2\pi(r - R_1)/(R_2 - R_1)]$. Constants a, b and c are arbitrarily chosen so that $\tilde{D} = 0$ and there are no disturbances at boundaries. A list of our numerically predicted f_{cr} and Re_{cr} (based on the inner radius, R_1, and its velocity, U_θ) and those from previous studies by other researchers is shown in table 1. Also shown in the table are results using finer grids. With higher resolution (up to 197×49), the difference in Re_{cr} is within 0.5% and an even better agreement for f_{cr} is achieved.

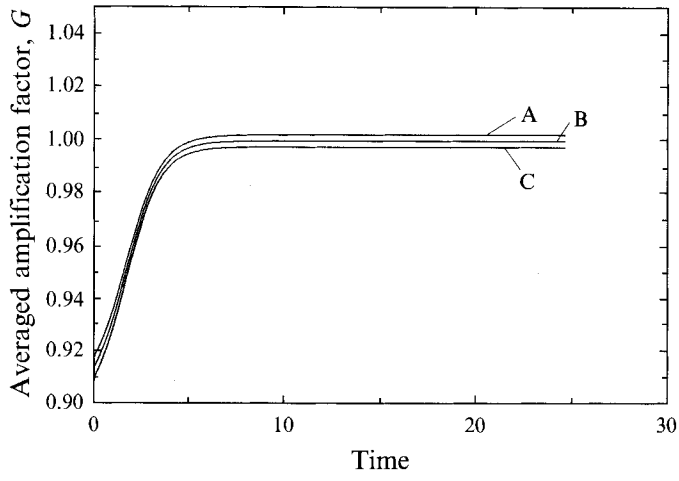

FIGURE 3. Averaged amplification factor. Wavenumber 3.2. Curve A, $Re = 75.0$, $G = 1.00224$; B, $Re = 72.5$, $G = 1.000962$; C, $Re = 70.0$, $G = 0.997726$.

	H (in.)	A (H/W)	V (r.p.m.)	Re $(\rho VD/2\mu)$	Fd $(2V^2/Dg)$	We $(2\sigma/\rho V^2 D)$
Case 1	1.728	0.864	50	17.17	0.0518	0.13274
Case 2	1.864	0.932	200	68.69	0.8280	0.00830
Case 3	2.0	1.0	420	144.248	3.3123	0.00188
Case 4	2.0714	1.0357	420	144.248	3.3123	0.00188

TABLE 2. The parameters of free-surface flows (see figure 4 for definitions of H, W, D and V)

At neutral stability points, the disturbances eventually evolve to fixed profiles as shown in figure 1(*a–c*). Each plot represents the development of the circumferential velocity disturbance in time corresponding to different initial conditions (i)–(iii) but the same neutrally stable values of Re and f. Owing to the nature of homogeneous problems, the solutions of the eigenproblems, i.e. the eigenfunctions, should have the same mode regardless of initial conditions with differences only in signs and amplitude. Curve C in figure 2(*a*, *b*) represents one of those eigenpoints. It can also be seen in figure 3 that the asymptotic value of the average amplification factor for the case of $(Re, f) = (72.5, 3.2)$ is the closest to 1 compared to other trial cases solved on the same grid (65×19). Among all the eigenpoints, the one with the smallest Re is determined to be the critical point, the physical onset of instability. The non-dimensional time shown in figures 2 and 3 is scaled by R_1/U. That is, one unit of non-dimensional time includes $1/(2\pi)$ of a cycle of revolution. All the numerical stability analyses were performed with a numerical time step of $1/72$ of a cycle in the total time period of four revolutions. It normally took 9–12 minutes on a SUN/Sparc-2 workstation to complete one task.

4. Experimental apparatus and procedure

Fluid flow experiments were conducted using a 11.5 in. long rectangular trough. The flows within the trough are driven by an internal rotating cylinder. The schematic of

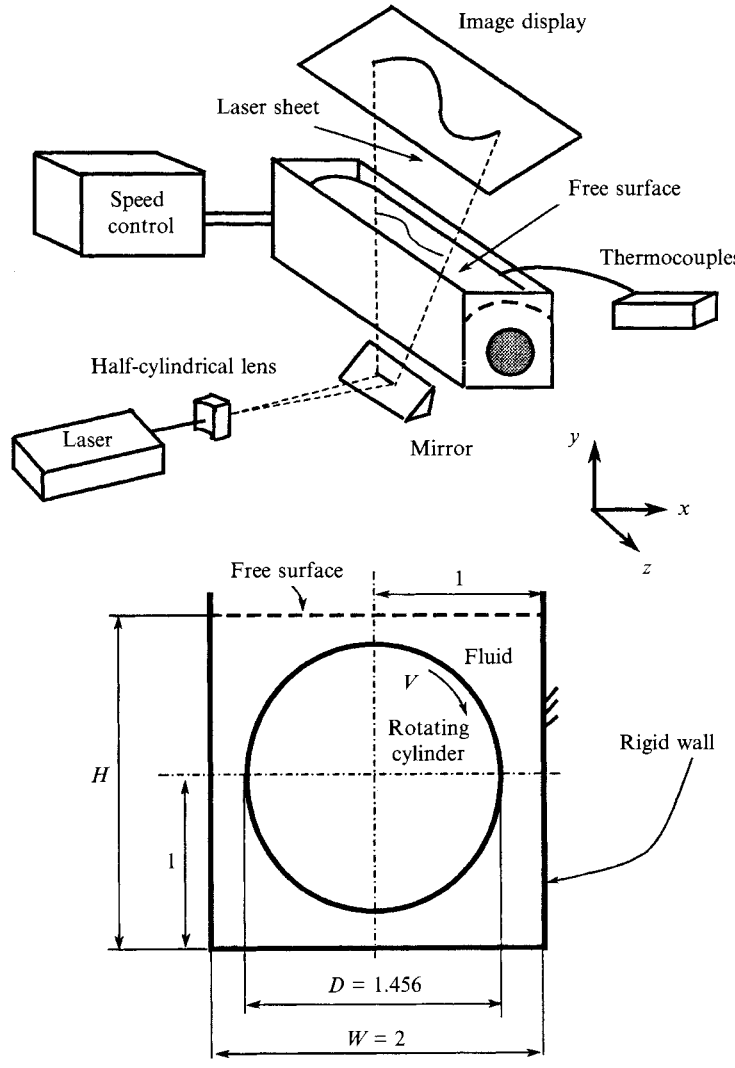

FIGURE 4. Schematic of the experimental set-up. Dimensions in inches.

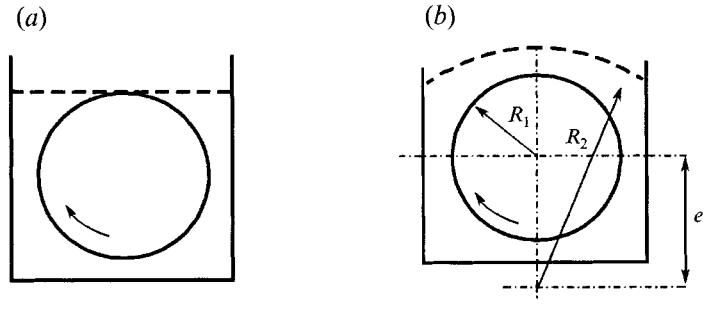

FIGURE 5. Initial condition for case 1: (*a*) $A = 0.864$, (*b*) $e = 2.15R_1$, $R_2 = 3.163R_1$.

the experimental set-up is shown in figure 4. During the experiments, attention was focused on three aspects: (i) to measure the free surface shape at steady state, (ii) to determine the critical parameters (i.e. Re_{cr} and f_{cr}), and (iii) to record the secondary

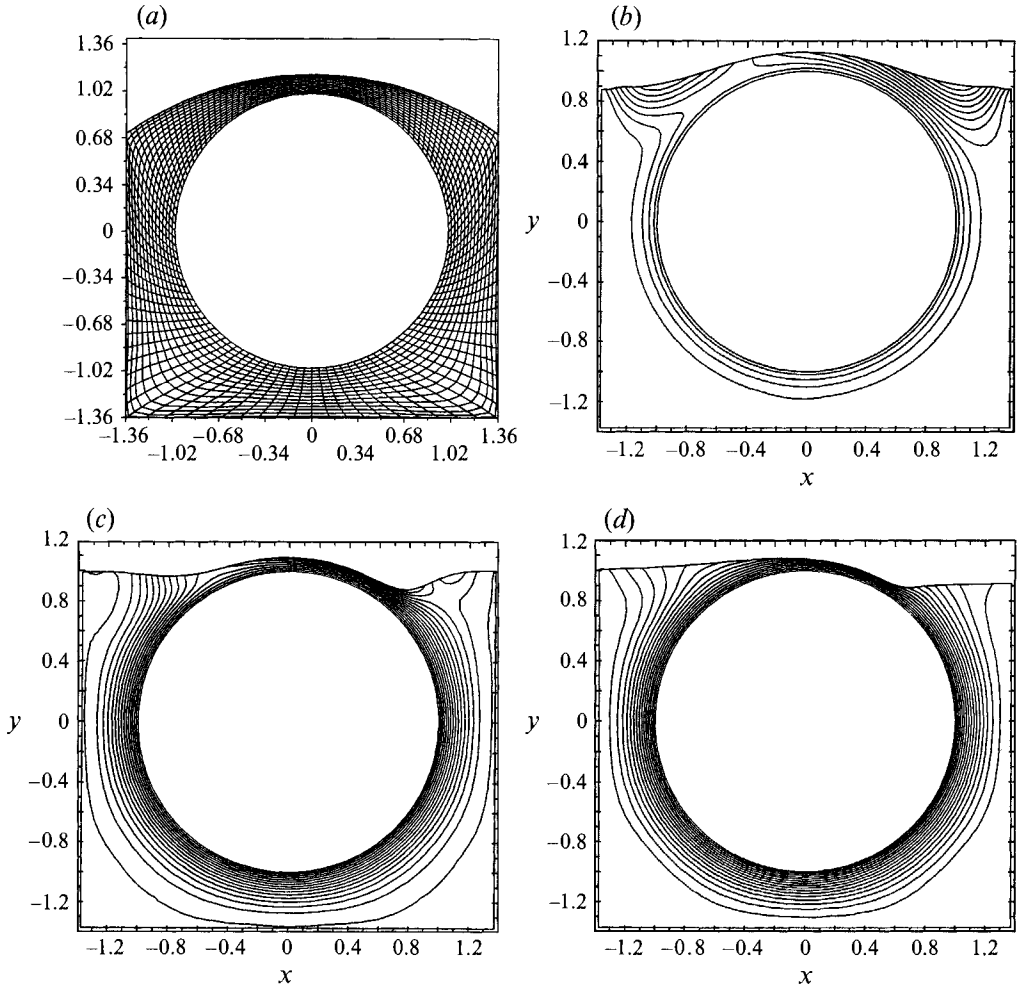

FIGURE 6(*a–d*). For caption see facing page.

flows from the top of the free surface by streak photography at an Re value higher than Re_{cr}.

The experimental apparatus is mounted on an optical table. The trough and the inner cylinder are made of a transparent material, Lucite. The rotation of the inner cylinder is controlled by a servo motor and the speed is measured by a digital tachometer (Shimpo, DT-205B) with accuracy to within one r.p.m. (in the range of 6–5000 r.p.m.). The experimental fluid is a clear silicon-based oil, Dow Corning 200 fluid. It has a surface tension coefficient of 22.08 dynes cm^{-1} and a specific gravity of 0.96 at 26 °C. Since the viscosity is rather temperature sensitive (see Appendix C), the temperature was carefully monitored and maintained at 26 °C to ensure a viscosity of 100 cP ($\pm 0.5\%$) throughout the experiment. For the flow visualization, suspended Kalliroscope flakes were used as scattering particles. The particles are made from guanine (density 1.62 g cm^{-3}) of size $6 \times 30 \times 0.07$ μm. Owing to their plate-like structure, the flakes can align themselves with the fluid flow; they have a refraction index of 1.85 which provides a good photographic contrast even in a very dilute concentration.

The height of the free surface is measured by a set of micrometers which can slide

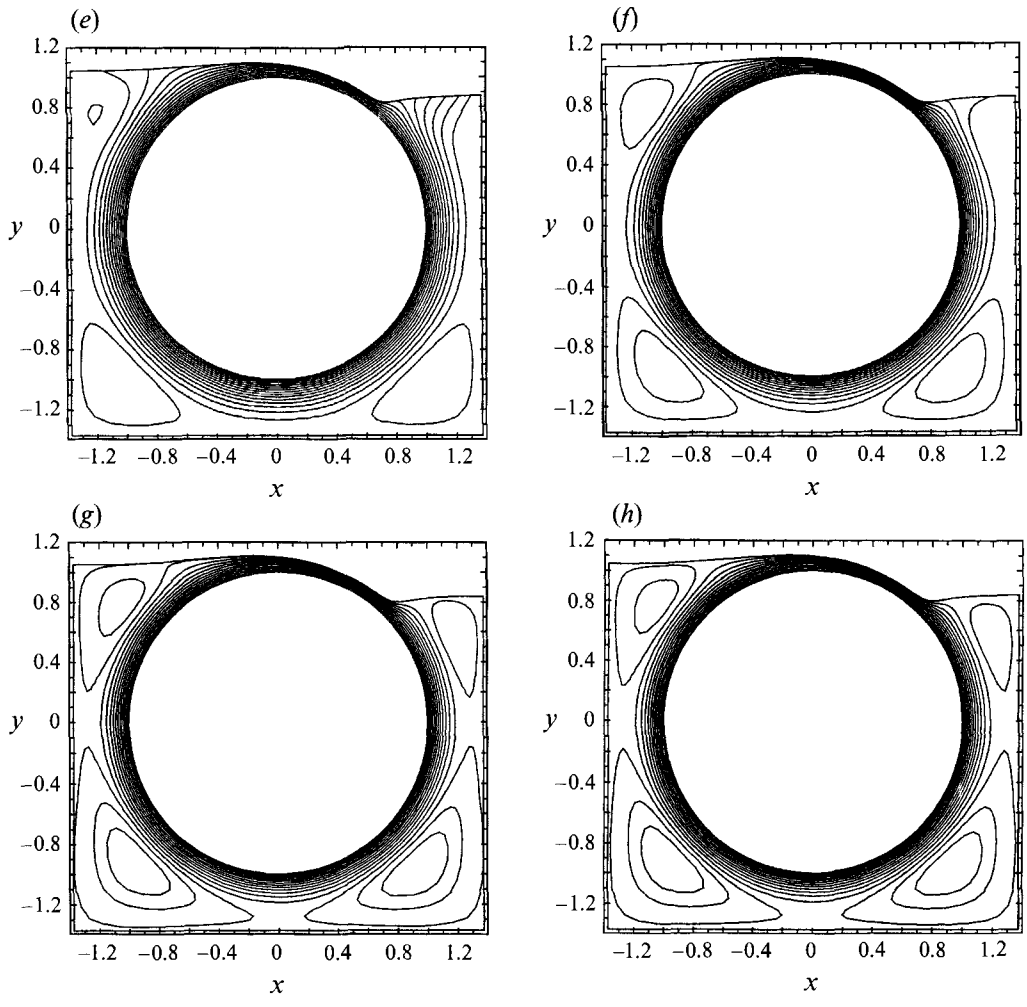

FIGURE 6. Transient solutions of case 1: (*a*) computational grid at t (dimensionless) = 0.2; (*b*) streamlines at $t = 0.2$, (*c*) $t = 0.5$, (*d*) $t = 1.0$, (*e*) $t = 1.5$, (*f*) $t = 2.0$, (*g*) $t = 2.5$, and (*h*) steady state.

along three perpendicular axes, x, y and z, with a pin attached at the bottom. By moving the micrometers across the trough in either the x- or z-direction (parallel to the table) while keeping the pin head barely in contact with the fluid, the surface shape in (x, y, z) can be measured.

A 12 mW helium–neon laser is used as light source for two purposes: to illuminate the scattering particles for flow visualization; and to help distinguish the onset of instability, which is determined by the appearance of top surface deformation. A thin sheet of laser light (approximate 1.5 mm thick, and several inches wide), expanded from a laser beam by a negative plano-cylindrical glass lens, is transmitted through the fluid from the bottom of the trough as shown in figure 4. The projected light sheet remains straight at the image display as long as the flow remains two-dimensional. Tiny free-surface deformation caused by axial motion can clearly lead to a wavy distortion of the laser sheet. It is sensitive enough to allow the determination of onset of instability to within 5 r.p.m. The critical parameters are obtained by taking the average of ten measurements.

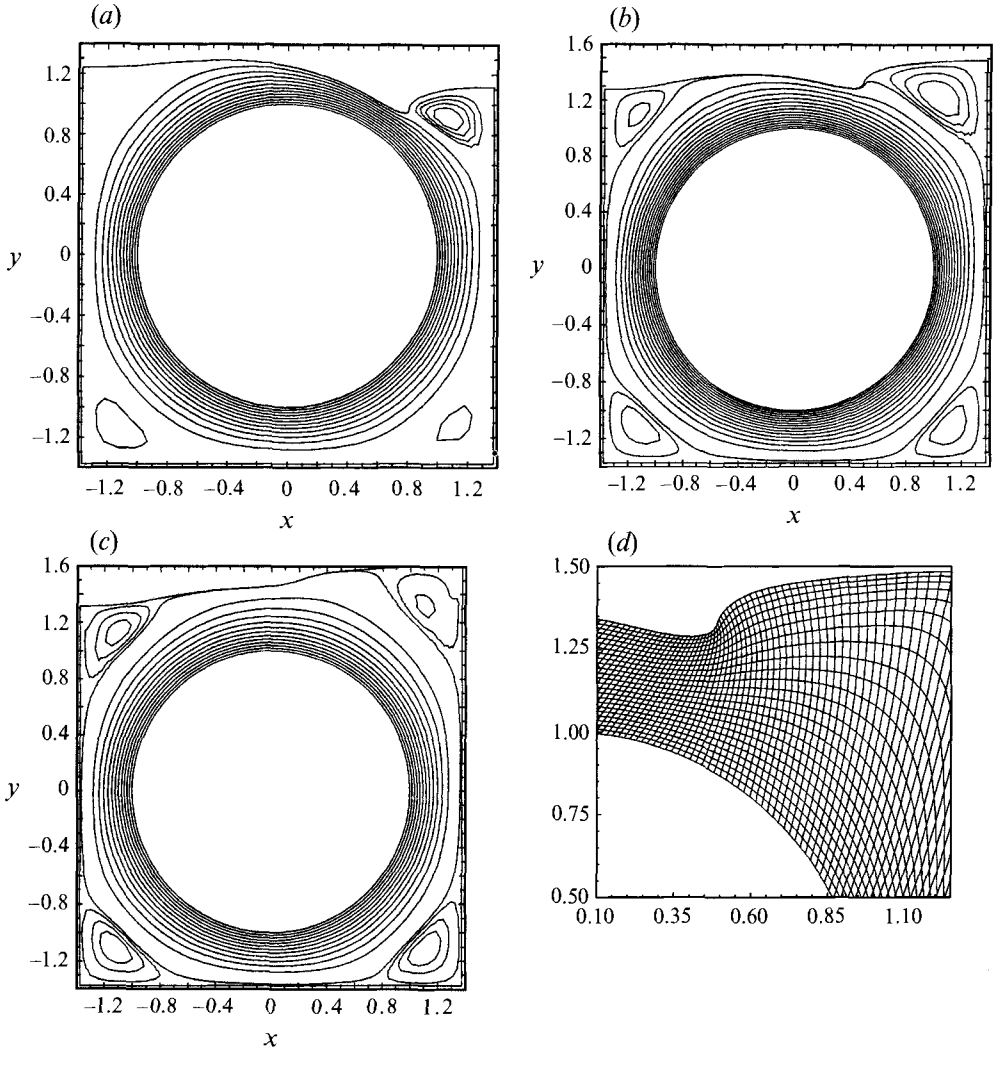

FIGURE 7. Steady-state solutions: (*a*) case 2, (*b*) case 3, (*c*) case 4 and (*d*) grid for case 3.

5. Results

In this section, a series of numerical simulations and experimental results is presented. Listed in table 2 are the four fluid flows, differentiated by the initial and boundary conditions.

The basic flows for all four cases were calculated in the first place and the stability for case 4 was further investigated. The results have been compared with experimental data for the two-dimensional free-surface shapes and Re_{cr}, f_{cr} of the secondary flow. The secondary flow, in terms of the wavy surface and the streak lines along the top free surface, has been numerically simulated to compare with photographs taken from the experiments. The characteristic length and speed were chosen to be $\frac{1}{2}D$ and V for the calculations.

5.1. *The basic flows*

In case 1, with a 0.864 aspect ratio (H/W), the initial level of the free surface could barely cover the inner roll as shown in figure 5(*a*). For simplicity, without changing the

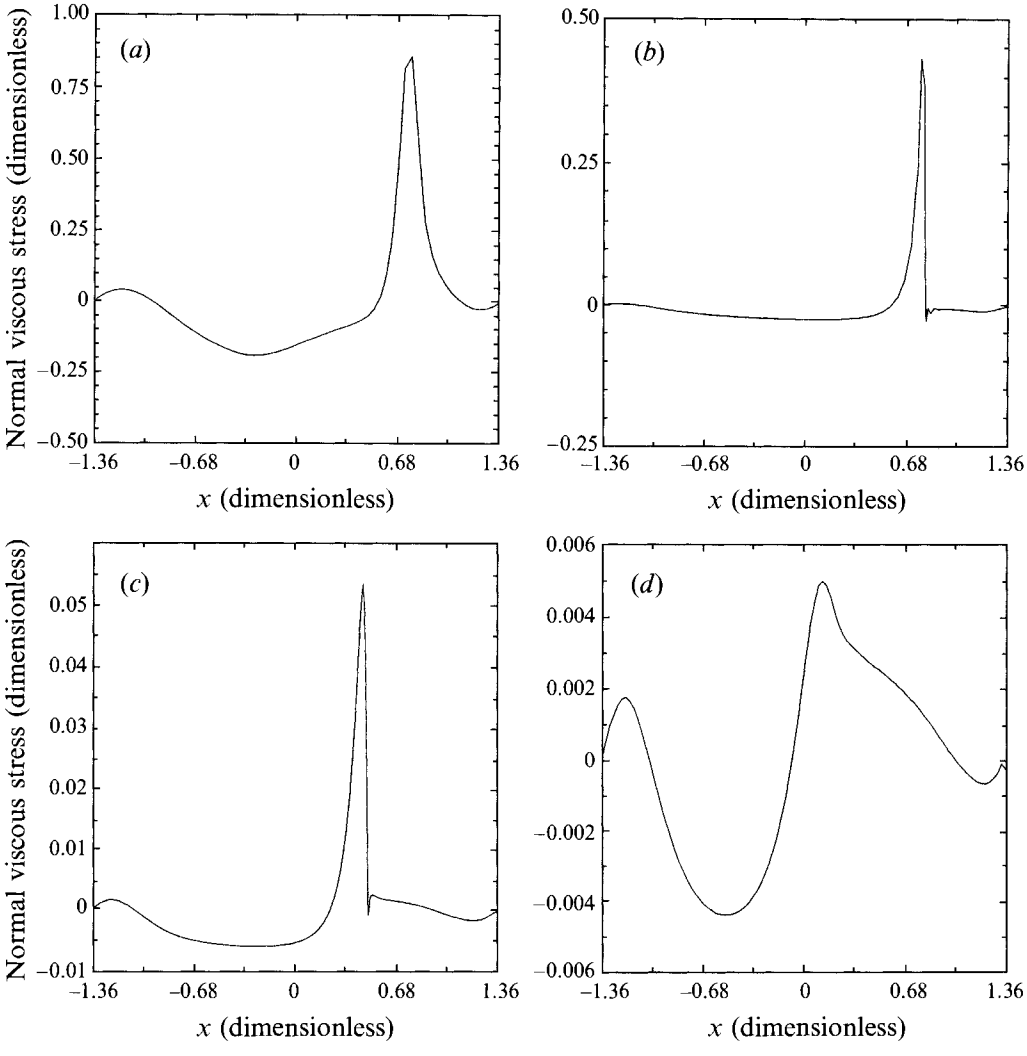

FIGURE 8. Distribution of normal viscous stress along the top free surfaces: (*a*) case 1, (*b*) case 2, (*c*) case 3, (*d*) case 4.

total amount of fluid, the initial shape of the free surface is assumed to be part of a circle as shown in figure 5(*b*). A 120 × 16 grid is used. For a higher numerical resolution on the free surface, half of the grid lines, i.e. 60 out of 120, are distributed along the free surface. The transient development, driven by the rotation of the inner cylinder under gravity, is shown in figure 6 by streamlines. Initially, $0 < t < 0.2$ ($t = d/2V$, is dimensionless), the flow is dominated by gravity. It can be clearly seen that the fluid over the middle part of the free surface is moving downward to the sides due to gravity. At $0.2 < t < 1.0$, as the viscous drag increases and the internal pressure builds up, the motion of the surface is quickly affected by the rotation and a height difference between the left (upstream) and the right surface (downstream) is established. Eventually, a separating streamline appears and reversed eddies form in each corner. A constant increment in stream function is chosen for all the streamline plots in figure 6.

The steady-state solutions for the other three cases are shown in figure 7, also by a stream-function distribution. To better show the flow patterns in the corners, the values of stream lines are not equally spaced (much smaller increments near the

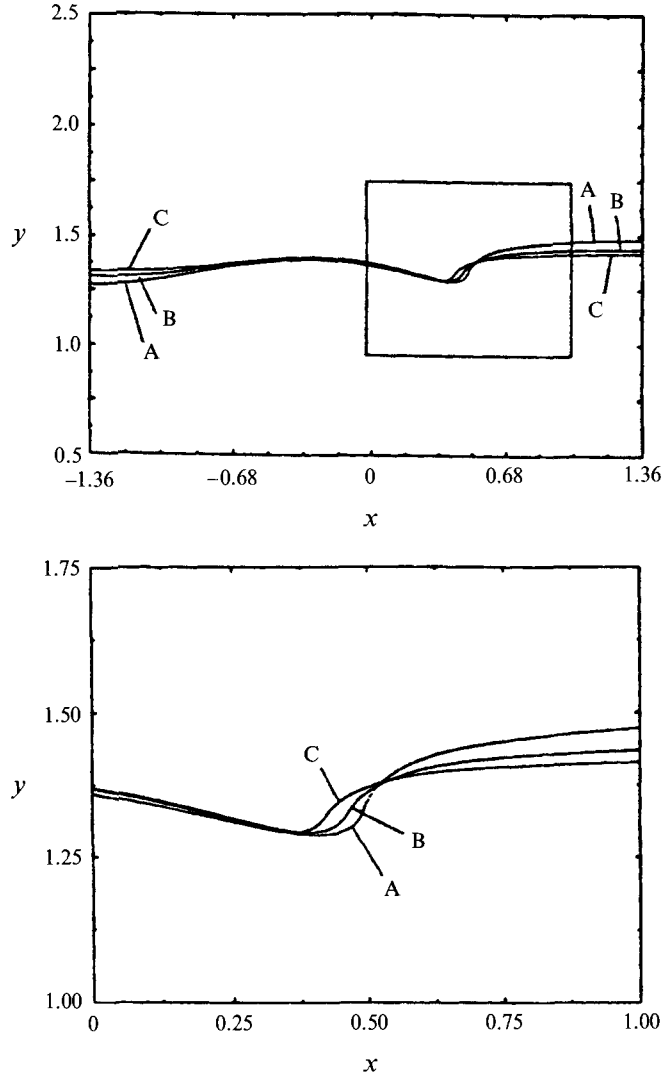

FIGURE 9. Free-surface shapes at steady states of case 3 for fluids with different viscosities: A, 100 cP; B, 50 cP; C, 25 cP.

corners). Note that since the Weber numbers of these three cases are smaller than case 1, the appearance of larger curvatures on the top surfaces are expected. Indeed, in cases 2 and 3 a pronounced local depression on the free surface has been observed in experiments and successfully predicted by calculations (see figure 10 also). However, in case 4, with further increases in the amount of fluid, no noticeable local depression can be seen. This can be explained by figure 8 where the distribution of normal viscous stresses along the free surfaces is plotted. In cases 2 and 3, the normal viscous stress increases rapidly to its peak value and vanishes. Surface tension will not be enough to counter the surging normal viscous stress without forming large curvatures. In case 4, the prominent spike of the normal viscous stress ceases to exist, so the surface depression no longer appears. Further increases in the rotational speeds in cases 2 or 3 would result in air entrainment through the surface depression. To further investigate the normal viscous stress effect in case 3, we changed the viscosity while maintaining the same rotational speed. In figure 9, the calculated surface shapes for three different

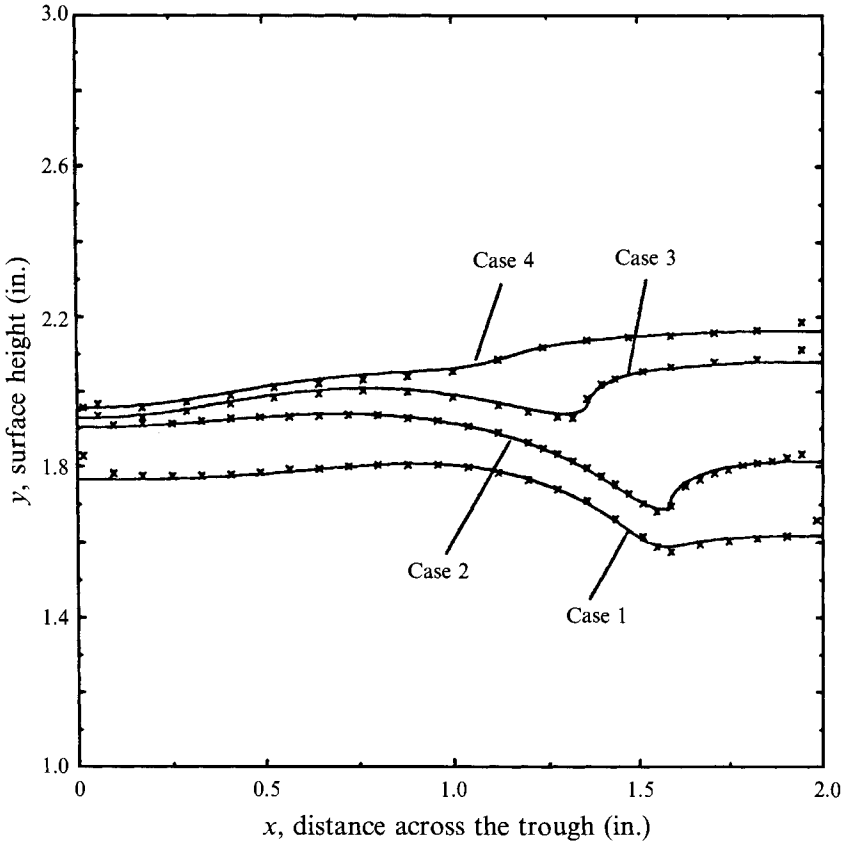

FIGURE 10. Free-surface shapes at steady states: comparison of numerical (——) and experimental (×) results.

values of viscosity are shown. Curve (*a*) corresponds to case 3 (100 cP) described above. Curves (*b*) and (*c*) represent the less viscous fluids, 50 and 25 cP respectively. The outcome of reducing viscosity is a decreases in curvature of the local depression. To better calculate the fluid flows of cases 2–4, a finer grid (196 × 25) was adopted with the use of an adaptive grid; That is the grid lines are clustered into the corners and near the free surface to improve the resolution in those areas. One example of grid clustering can be seen in figure 7(*d*). It has been found that the clustering is critical for cases 2 and 3 in seeking accurate solutions, due to the substantial curvature change.

Displayed in figure 10 are the numerical calculations and the measured free-surface shapes, taken at the middle of the trough (for smaller end effects). The experimental errors are estimated to be ± 0.015 in. in the y-direction (normal to the free surface), and ± 0.004 in. in the x-direction. The higher error in the normal direction is due to the capillary effect, which occurs when the micrometer pin moves vertically in order to contact the free surface. Excellent agreement was obtained for all four cases, except near the rigid walls due to the capillary effect which is not considered in the model. For simplicity, the angles of attachment were assumed to be 90° in the calculations.

5.2. *The secondary flow: free-surface Taylor vorticies*

The flow instability of case 4 was investigated in a fashion similar to the previous study of concentric Taylor–Couette flow. The only difference is that the free-surface shape must be perturbed along with the other flow variables according to (2.12) and solved

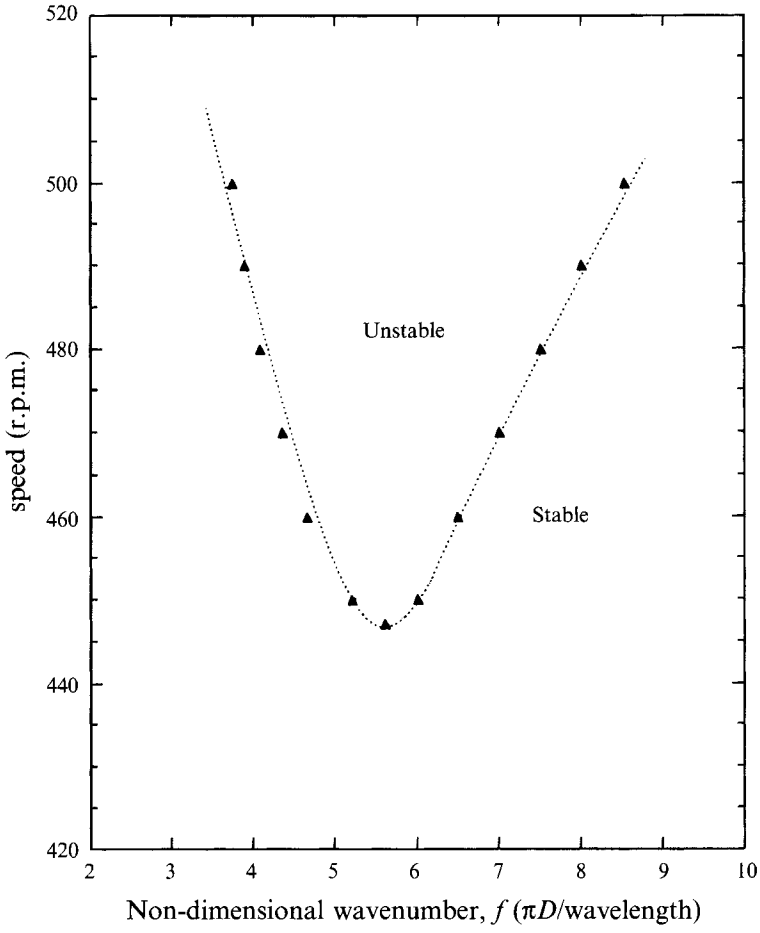

FIGURE 11. Stability map (experimental errors are estimated to be $\pm 2\%$ in wavenumber, and ± 5 r.p.m. in rotational speed.) ▲, Numerically determined neutral stability points.

Measurement number	Critical speed (r.p.m.)	Critical wavenumber	Measurement number	Critical speed (r.p.m.)	Critical wavenumber
1	438	5.72	6	432	5.51
2	445	5.58	7	434	5.58
3	443	5.51	8	440	5.38
4	439	5.65	9	436	5.79
5	437	5.65	10	441	5.51

	Critical speed (r.p.m.)	Critical wavenumber (f_{cr})
Average of measurements	438.5	5.59
Numerical simulation	447	5.60

TABLE 3. Experimental *vs.* numerical results

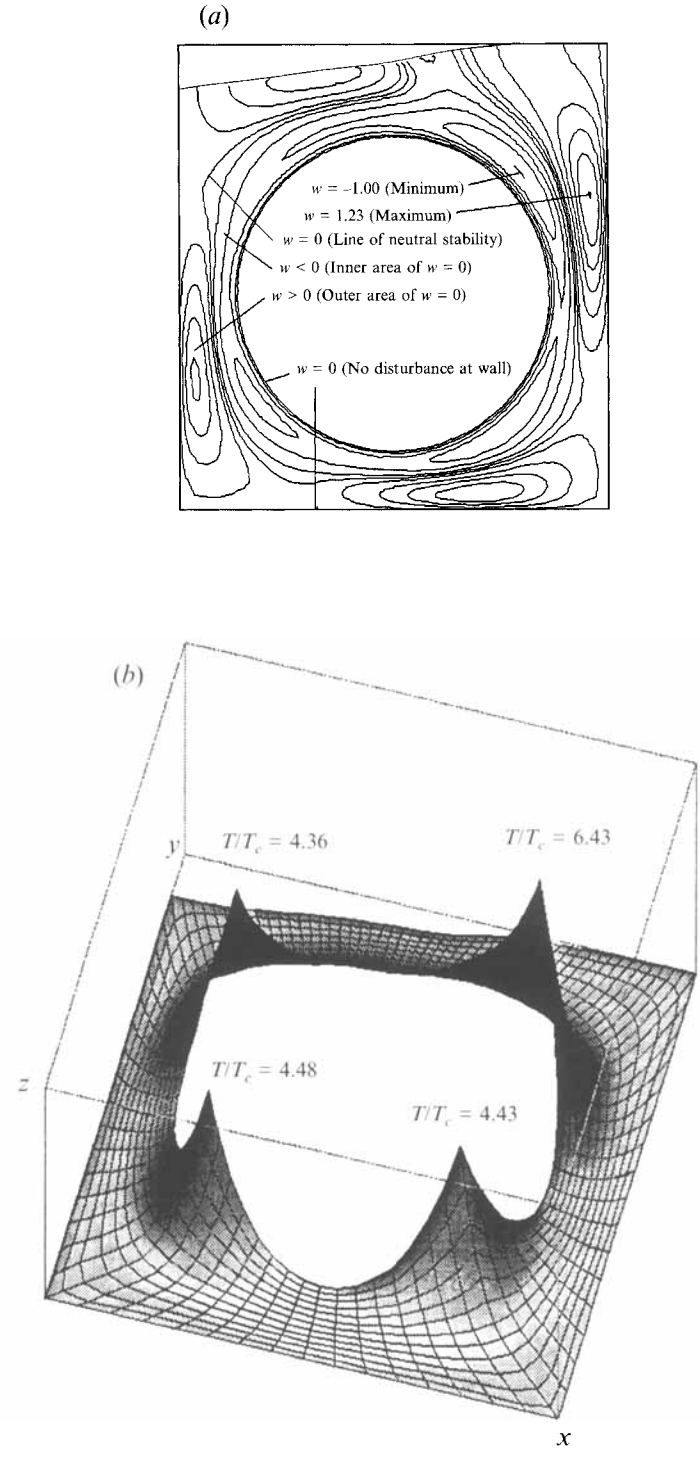

FIGURE 12. (*a*) Axial velocity disturbance, w. (*b*) Normalized local Taylor number, T/T_c. $T = (Ud/\nu)^2 (d/R)\ (\eta/(1+\eta))$, $\eta = R/(R+d)$. U, d R, ν are the local velocity, gap width, inner radius and kinematic viscosity. T is the local Taylor number of free-surface Taylor flow. T_c is the corresponding critical Taylor number (DiPrima & Swinney 1981) for concentric Taylor flows with same value of η.

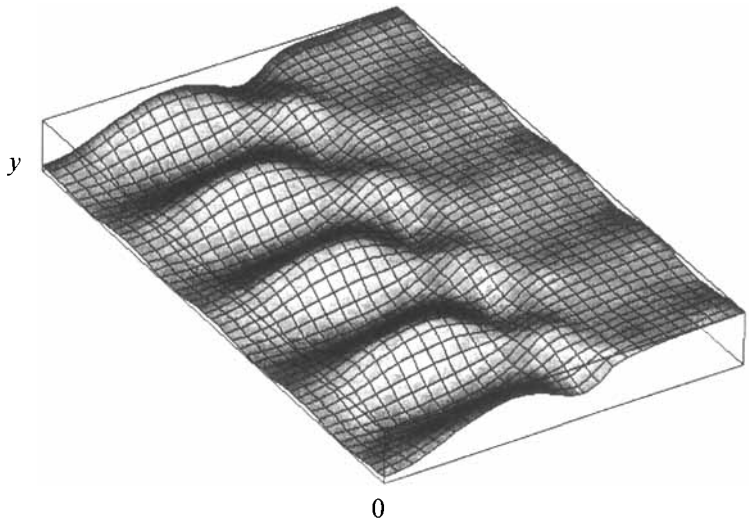

FIGURE 13. Deformed free surface.

for as an unknown. The computational domain in use is the fixed geometry obtained from the precalculated steady-state solution of the basic flow. The disturbance of the free-surface shape affects the secondary flow through the boundary conditions, (2.13*f*, *g*) and (2.14b). The disturbed viscous stress and pressure are hence influenced by the perturbation of the free-surface shape, and vice versa.

In order to perform the stability analysis, a number of precalculated basic flows are required. The computations have been done in the speed range of 420 to 500 r.p.m. Figure 11 shows the stability map derived from the numerical calculation.

The critical point was determined, among other neutral stability points, to be $(Re, \lambda) = (447$ r.p.m., 5.60). As shown in table 3, they match well with the experimental data, which are averages of ten sets of experimental results. It should be stated that since the wavenumber (or the wavelength) at a higher rotation speed does not vary from that at the onset of instability, the measurements of wavenumbers are actually taken around 500 r.p.m. The experiments show that the end effect seems to destabilize the flows since the secondary flow always begins at the ends. Therefore, the calculated critical speed ought to be higher than the measured one.

To visualize the perturbed flow field, a contour plot of w, the normal mode of axial velocity disturbance, is drawn in the (x, y) domain. Figure 12(*a*) shows that the fluid in each of the converging regions has developed a prominent secondary flow. The largest disturbance is not near the free surface but is in the upper right corner where the circumferential flow must change most rapidly. It also has been observed from the calculations that the two- and three-dimensional solutions are not much affected by the variation in surface tension and certainly not as much as they are by the Reynolds number. Therefore, we believe that, in contrast to the Kelvin–Helmholtz instability, the disturbance of the free surface is not a dominant effect as regards flow instability. Instead, this secondary flow, even with a free surface, is similar to the Taylor vortices between two concentric cylinders where the instability is determined by flow inertial. The concept of the present instability being inertia driven is made more apparent by examining the local Taylor number distribution, as shown in figure 12(*b*). By superimposing the three-dimensional solutions onto the two-dimensional ones, the secondary flows can be approximated. It can be seen that the present instability occurs

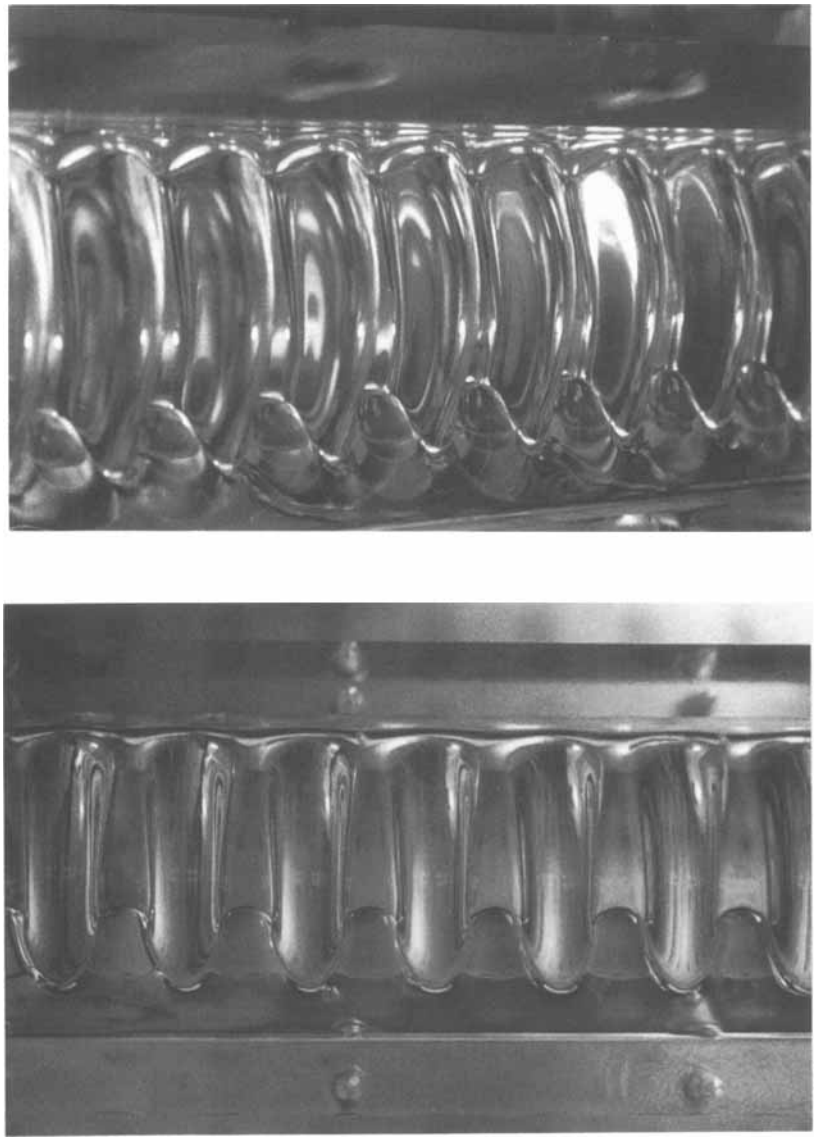

FIGURE 14. Free surface of the secondary flow for case 3 at $V = 500$ r.p.m.

when the maximum local Taylor number (maximum $T/T_c = 6.43$) is supercritical. In addition, the largest perturbation occurs in the area of maximum local Taylor number.

Similarly, superimposing the disturbance of the free surface shape at the onset of instability onto the basic shape, the deformed surface due to the secondary flow can be approximated. In figure 13, the deformed surface with four cells is plotted. The photographs of the real flows are shown in figure 14.

It should be noted that based on the linear stability analysis, the solution variables, (u, v, w, h), of the perturbation equations are the normal modes of the amplitudes of disturbances, (u', v', w', h'). In superimposing on two-dimensional solutions, the amplitude of disturbances is chosen in such a way that, for example, it can provide a trajectory plot close enough to the experimental result obtained at supercritical *Re* as

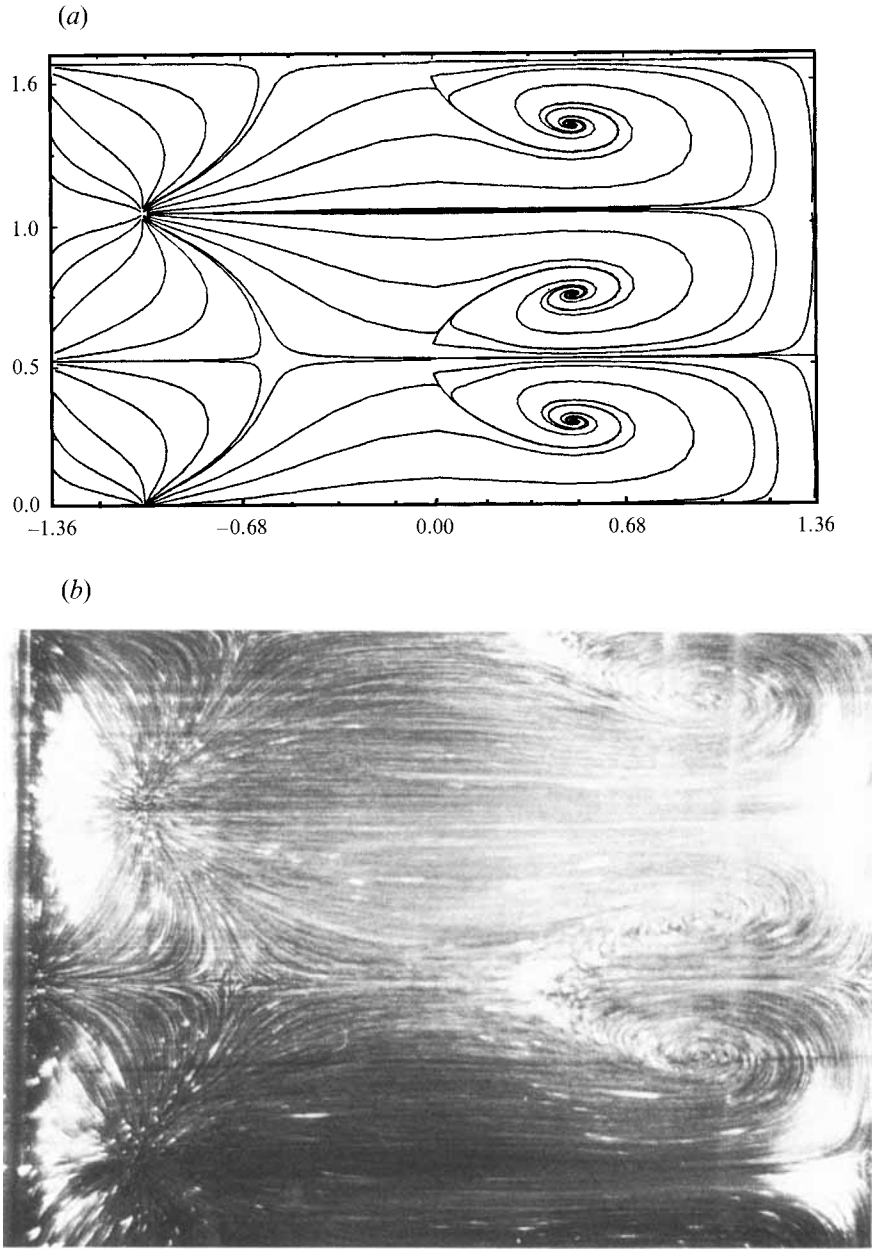

FIGURE 15. (*a*) Simulation, (*b*) photograph of streak lines near the free surface.

shown in figure 15. It is obvious that to simulate the supercritical flows in this way without real three-dimensional computation is only a qualitative approximation. It becomes even less informative as the flow becomes more supercritical. Deviation is expected not only because the photo was taken at the supercritical state but also because the flow trajectories were calculated exactly on the free surface, while the photographic streak lines involves trajectories some distance below the surface, especially in the higher (in y) side of the downstream region where a sink-like structure under the free surface tends to be displaced toward the right wall. In general, however, figure 15 shows that by properly choosing the amplitude the important feature of the

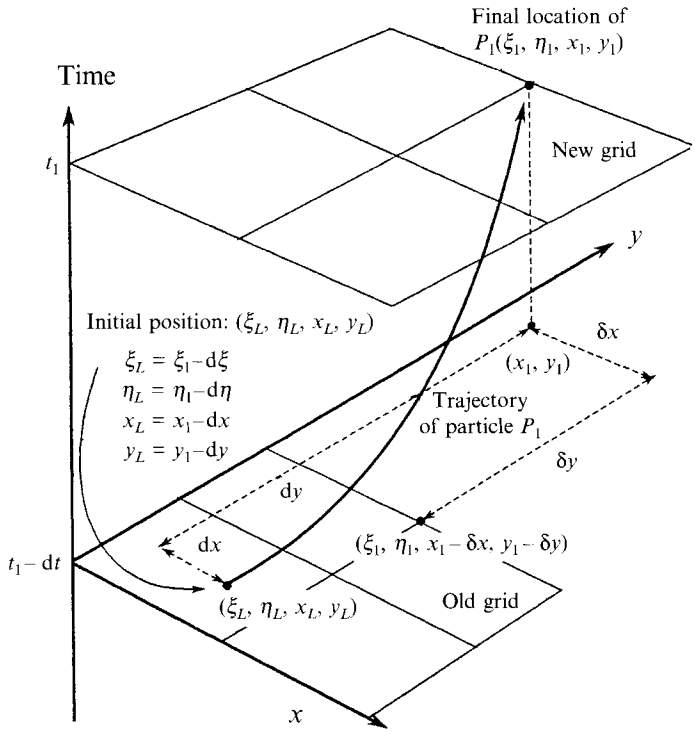

FIGURE 16. Spatial–time system for time-varying coordinates.

supercritical free-surface Taylor flow at 500 r.p.m. can be revealed by the linear analysis conducted at neutrally stable point at 447 r.p.m.

A closer look at the secondary flow from top free surface shows that it is characterized by a cellular pattern with the highest speed in the centre, directly over the rotating cylinder. There appears to be an upwelling (source-like) of fluid on the left in the centre of each cell. A portion of the flow travels back toward the left wall while the rest follows in the direction of the rotation of the internal cylinder toward the right. Two surface eddies, rotating in opposite directions, are formed on the right side of the cell where the trajectories all converge, resulting in a spiralling sink-like behaviour. The pair of eddies in each cell jointly form a tongue-shaped feature near the middle of the cell. At the upstream (left) side, separating streamlines together with the surface stagnation points are seen in the trajectories dividing the flow issuing from the surface source travelling to the left wall from that travelling to the eddies.

6. Summary

Free-surface Taylor vortex flow is studied both numerically and experimentally. This flow, similar to Taylor–Couette flows between two cylinders, bifurcates from two-dimensional flow into a three-dimensional flow pattern as the Reynolds number is increased beyond the critical value. The strikingly periodic variation of the free-surface shape makes this flow structure distinct from the usual enclosed Taylor vortex flow. Because of its complex but ordered flow field in both the basic and secondary flows, this flow structure offers an ideal case for flow visualization as well as numerical simulation. Four cases of basic flows with different initial and boundary conditions have been simulated. All the numerical results compared well with the measurements

of the two-dimensional surface shapes at steady state. The appearance of a local depression in the free surface has been explained on the basis of the large normal viscous stress gradients developed in the flow on the free surface. Based on one of the calculated basic solutions, numerical stability analysis is performed and the onset of free-surface Taylor vortex flow is successfully predicted in terms of the critical wavenumber and Reynolds number. At the neutral stability point, by superimposing the disturbances onto the basic flow, the secondary flow field can be approximately reconstructed. From flow visualization, the existence of the numerically predicted source–sink-like flow field near the top surface has been confirmed. Since the linearized equations for disturbances are solved as an initial value problem, one advantage of this method is its ability to treat time-varying systems for both the basic flows and the secondary flows. Only stationary flows, however, are involved in the present study.

The authors would like to thank Dr Juris Privics of Xerox Webster Research Center/Mechanical Engineering Science Laboratory for supporting this work and both H. Metternich and G. Bay for their work in fabricating the experimental apparatus.

Appendix A. Eulerian–Lagrangian method

An implicit Eulerian–Lagrangian method using linear interpolation in moving-boundary-fitted coordinates is developed. Using (2.9*a*) for example (subscript 1 is removed for simplicity), splitting the inertia term by Eulerian–Lagrangian method and moving the unknown, u (the unknown to be solved), to the left-hand side, the equation becomes

$$J\nabla^2 u - Re\, J\left(\frac{u}{\Delta t}\right) = Re\left\{J\left(\frac{-u_L}{\Delta t}\right) + (y_\eta P)_\xi - (y_\xi P)_\eta\right\}, \tag{A 1}$$

where u_L is the x-component of U_L, the velocity of the same fluid particle at $t-\Delta t$ from the Lagrangian point of view.

To obtain U_L fluid trajectories need to be calculated. since the particles located on a mesh node at time t do not necessarily initiate from a node at time $t-\Delta t$, interpolation is needed. By using boundary-fitted coordinates, the process of interpolation is performed quite simply on a square grid compared to an irregular one. This is another advantage of using boundary-fitted coordinates. However, in free-surface problems since the grids are always changing, i.e. the same coordinates in the (ξ, η)-domain at different time steps could represent different physical positions, extra attention must be paid to interpolation for U_L.

Consider a spatial–time coordinate system, figure 16, employed in a time-marching scheme. Two sets of grids are shown at two consecutive time steps with interval $\mathrm{d}t$. Note that the grid has been redistributed from time $t_1-\mathrm{d}t$ to time t_1 due to the movement of the boundaries. If the velocity distributions $U(\xi, \eta, t_1)$ and $U(\xi, \eta, t_1-\mathrm{d}t)$ are known, then the trajectory during time $\mathrm{d}t$ of an arbitrary particle, P_1 for example, can be derived. Accordingly, U_L can be obtained by interpolating from $U(\xi, \eta, t_1-\mathrm{d}t)$. Let $(\mathrm{d}\xi, \mathrm{d}\eta)$ be the values of displacements of P_1 in the curvilinear coordinate system within duration $\mathrm{d}t$. And correspondingly $(\mathrm{d}x, \mathrm{d}y)$ are the values in Cartesian coordinates. The values of $(\mathrm{d}x, \mathrm{d}y)$ can be approximated by

$$\frac{\mathrm{d}x}{\mathrm{d}t} = u, \quad \frac{\mathrm{d}y}{\mathrm{d}t} = v, \quad \mathrm{d}x = 0.5\,(u+u_L), \quad \mathrm{d}y = 0.5(v+v_L).$$

The relation between $(\mathrm{d}\xi, \mathrm{d}\eta)$ and $(\mathrm{d}x, \mathrm{d}y)$ is, by the chain rule,

$$\mathrm{d}\xi = \xi_x \mathrm{d}x + \xi_y \mathrm{d}y + \xi_t \mathrm{d}t = \xi_1 - \xi_L, \tag{A 2a}$$

$$\mathrm{d}\eta = \eta_x \mathrm{d}x + \eta_y \mathrm{d}y + \eta_t \mathrm{d}t = \eta_1 - \eta_L, \tag{A 2b}$$

where the grid speed (ξ_t, η_t) can be obtained from

$$\delta\xi = \xi_x \delta x + \xi_y \delta y + \xi_t \delta t = 0 \quad \text{along constant } \xi \text{ curve}, \tag{A 3a}$$

$$\delta\eta = \eta_x \delta x + \eta_y \delta y + \eta_t \delta t = 0 \quad \text{along constant } \eta \text{ curve}, \tag{A 3b}$$

in which the $(\delta x, \delta y)$ are the differences of the coordinate values of x and y of each grid node between the two grids, which have a time interval δt. Choose δt to be equal to $\mathrm{d}t$, and combine (A 2) and (A 3) to obtain

$$\mathrm{d}\xi = [y_\eta(\mathrm{d}x - \delta x) + x_\eta(\delta y - \mathrm{d}y)]/J, \tag{A 4a}$$

$$\mathrm{d}\eta = [y_\xi(\delta x - \mathrm{d}x) + x_\eta(\mathrm{d}y - \delta y)]/J. \tag{A 4b}$$

Once $(\mathrm{d}\xi, \mathrm{d}\eta)$ are derived, (ξ_L, η_L) can be determined from (A 2). Accordingly, U_L can be interpolated from $U(\xi, \eta, t_1 - \mathrm{d}t)$ at neighbouring nodes. In this study, linear interpolation was used. Notice that the above procedure should be applied iteratively to calculate U_L and the trajectories until all the unknowns above have converged.

Appendix B. Consistent discretization

The difficulty of solving the pressure equation, (2.10), with just the Neumann boundary condition comes from the compatibility condition (divergence theorem) which relates the Neumann boundary condition and the source term of the Poisson equation for pressure. The two-dimensional form of the divergence theorem is

$$\iint_A \nabla^2 f \, \mathrm{d}A - \oint_L \frac{\partial f}{\partial n} \mathrm{d}L = 0, \tag{B 1}$$

where L is the complete boundary and A is the area within it. If (2.10*a–c*) (assume no free surface) fail to satisfy this criterion, no numerical solution can be obtained. Consider a singly connected region in the (ξ, η)-plane with $(m-1)\times(n-1)$ square-meshed grids inside. Equation (2.10*a*) is solved with boundary condition (2.10*b*) on $\xi = 1$, $\xi = m$, and (2.10*c*) on $\eta = 1$, $\eta = n$. Discretize the left-hand side of (2.10*a*) using (2.13), then

$$\begin{aligned}
\text{LHS (2.10}a\text{)} = &\left[\left\{\frac{1}{J} y_\eta \left[(y_\eta p)_\xi - (y_\xi p)_\eta\right]\right\}_{i+1/2,j} - \left\{\frac{1}{J} y_\eta \left[(y_\eta p)_\xi - (y_\xi p)_\eta\right]\right\}_{i-1/2,j}\right] \Big/ \Delta\xi \\
&- \left[\left\{\frac{1}{J} x_\eta \left[-(x_\eta p)_\xi + (x_\xi p)_\eta\right]\right\}_{i+1/2,j} - \left\{\frac{1}{J} x_\eta \left[-(x_\eta p)_\xi + (x_\xi p)_\eta\right]\right\}_{i-1/2,j}\right] \Big/ \Delta\xi \\
&- \left[\left\{\frac{1}{J} y_\xi \left[(y_\eta p)_\xi - (y_\xi p)_\eta\right]\right\}_{i,j+1/2} - \left\{\frac{1}{J} y_\xi \left[(y_\eta p)_\xi - (y_\xi p)_\eta\right]\right\}_{i,j-1/2}\right] \Big/ \Delta\eta \\
&+ \left[\left\{\frac{1}{J} x_\xi \left[-(x_\eta p)_\xi + (x_\xi p)_\eta\right]\right\}_{i+1/2,j} - \left\{\frac{1}{J} x_\xi \left[-(x_\eta p)_\xi + (x_\xi p)_\eta\right]\right\}_{i-1/2,j}\right] \Big/ \Delta\eta.
\end{aligned}$$

And the right-hand side is

$$\mathrm{RHS}(2.10a) = \left[\left\{x_\eta\left(\frac{\mathrm{d}v}{\mathrm{d}t}\right) - y_\eta\left(\frac{\mathrm{d}u}{\mathrm{d}t}\right)\right\}_{i+1,j} - \left\{x_\eta\left(\frac{\mathrm{d}v}{\mathrm{d}t}\right) - y_\eta\left(\frac{\mathrm{d}u}{\mathrm{d}t}\right)\right\}_{i-1,j}\right] \Big/ 2\Delta\xi$$
$$+ \left[\left\{-x_\xi\left(\frac{\mathrm{d}v}{\mathrm{d}t}\right) + y_\xi\left(\frac{\mathrm{d}u}{\mathrm{d}t}\right)\right\}_{i,j+1} - \left\{-x_\xi\left(\frac{\mathrm{d}v}{\mathrm{d}t}\right) + y_\xi\left(\frac{\mathrm{d}u}{\mathrm{d}t}\right)\right\}_{i,j-1}\right] \Big/ 2\Delta\eta,$$

where $2 \leqslant i \leqslant m-1, 2 \leqslant j \leqslant n-1$. The x- and y-coordinates at mid-points are derived by linear interpolation from neighbouring integer nodes, and all the first-order derivatives are calculated by central difference using points from both sizes half a mesh away. For example,

$$y_{i+1/2,j} = \tfrac{1}{2}(y_{i+1,j} + y_{i,j}), \quad y_{i+1/2,j-1/2} = \tfrac{1}{4}(y_{i+1,j} + y_{i+1,j-1} + y_{i,j-1} + y_{i,j}),$$
$$(y_\xi)_{i,j+1/2} = (y_{i+1/2,j+1/2} - y_{i-1/2,j+1/2})/\Delta\xi, \quad [(y_\xi p)_\eta]_{i,j+1/2} = [(y_\xi p)_{i,j+1} - (y_\xi p)_{i,j}]/\Delta\eta.$$

In order to satisfy the compatibility criterion, boundary conditions (2.10b, c) have to be discretized consistently and therefore evaluated at half a mesh away from the boundary. Use (2.14a, b) to evaluate the left-hand side of (2.10b, c):

$$\mathrm{LHS}(2.10b)\ |_{\xi=1} = \left\{\frac{1}{J} y_\eta [(y_\eta p)_\xi - (y_\xi p)_\eta]\right\}_{1+1/2,j} - \left\{\frac{1}{J} x_\eta [-(x_\eta p)_\xi + (x_\xi p)_\eta]\right\}_{1+1/2,j},$$

$$\mathrm{LHS}(2.10b)\ |_{\xi=m} = \left\{\frac{1}{J} y_\eta [(y_\eta p)_\xi - (y_\xi p)_\eta]\right\}_{m-1/2,j} - \left\{\frac{1}{J} x_\eta [-(x_\eta p)_\xi + (x_\xi p)_\eta]\right\}_{m-1/2,j},$$

$$\mathrm{LHS}(2.10c)\ |_{\eta=1} = \left\{\frac{1}{J} x_\xi [-(x_\eta p)_\xi + (x_\xi p)_{\xi\eta}]\right\}_{i,1+1/2} - \left\{\frac{1}{J} y_\xi [(y_\eta p)_\xi - (y_\xi p)_\eta]\right\}_{i,1+1/2},$$

$$\mathrm{LHS}(2.10c)\ |_{\eta=n} = \left\{\frac{1}{J} x_\xi [-(x_\eta p)_\xi + (x_\xi p)_\eta]\right\}_{i,n-1/2} - \left\{\frac{1}{J} y_\xi [(y_\eta p)_\xi - (y_\xi p)_\eta]\right\}_{i,n-1/2}.$$

And the right-hand side in discrete form is:

$$\mathrm{RHS}(2.10b)\ |_{\xi=1} = 0.5\left\{x_\eta\left(\frac{\mathrm{d}v}{\mathrm{d}t}\right) - y_\eta\left(\frac{\mathrm{d}u}{\mathrm{d}t}\right)_\eta - \frac{1}{Re}\omega_\eta + x_\eta\frac{1}{Fd}\right\}_{1,j}$$
$$+ 0.5\left\{x_\eta\left(\frac{\mathrm{d}v}{\mathrm{d}t}\right) - y_\eta\left(\frac{\mathrm{d}u}{\mathrm{d}t}\right)_\eta - \frac{1}{Re}\omega_\eta + x_\eta\frac{1}{Fd}\right\}_{2,j},$$

$$\mathrm{RHS}(2.10b)\ |_{\xi=m} = 0.5\left\{x_\eta\left(\frac{\mathrm{d}v}{\mathrm{d}t}\right) - y_\eta\left(\frac{\mathrm{d}u}{\mathrm{d}t}\right)_\eta - \frac{1}{Re}\omega_\eta + x_\eta\frac{1}{Fd}\right\}_{m,j}$$
$$+ 0.5\left\{x_\eta\left(\frac{\mathrm{d}v}{\mathrm{d}t}\right) - y_\eta\left(\frac{\mathrm{d}u}{\mathrm{d}t}\right)_\eta - \frac{1}{Re}\omega_\eta + x_\eta\frac{1}{Fd}\right\}_{m-1,j},$$

$$\mathrm{RHS}(2.10c)\ |_{\eta=1} = 0.5\left\{-x_\xi\left(\frac{\mathrm{d}v}{\mathrm{d}t}\right) + y_\xi\left(\frac{\mathrm{d}u}{\mathrm{d}t}\right)_\eta + \frac{1}{Re}\omega_\xi - x_\xi\frac{1}{Fd}\right\}_{i,1}$$
$$+ 0.5\left\{-x_\xi\left(\frac{\mathrm{d}v}{\mathrm{d}t}\right) + y_\xi\left(\frac{\mathrm{d}u}{\mathrm{d}t}\right)_\eta + \frac{1}{Re}\omega_\xi - x_\xi\frac{1}{Fd}\right\}_{i,2},$$

$$\mathrm{RHS}(2.10c)\ |_{\eta=n} = 0.5\left\{-x_\xi\left(\frac{\mathrm{d}v}{\mathrm{d}t}\right) + y_\xi\left(\frac{\mathrm{d}u}{\mathrm{d}t}\right)_\eta + \frac{1}{Re}\omega_\xi - x_\xi\frac{1}{Fd}\right\}_{i,n}$$
$$+ 0.5\left\{-x_\xi\left(\frac{\mathrm{d}v}{\mathrm{d}t}\right) + y_\xi\left(\frac{\mathrm{d}u}{\mathrm{d}t}\right)_\eta + \frac{1}{Re}\omega_\xi - x_\xi\frac{1}{Fd}\right\}_{i,n-1}.$$

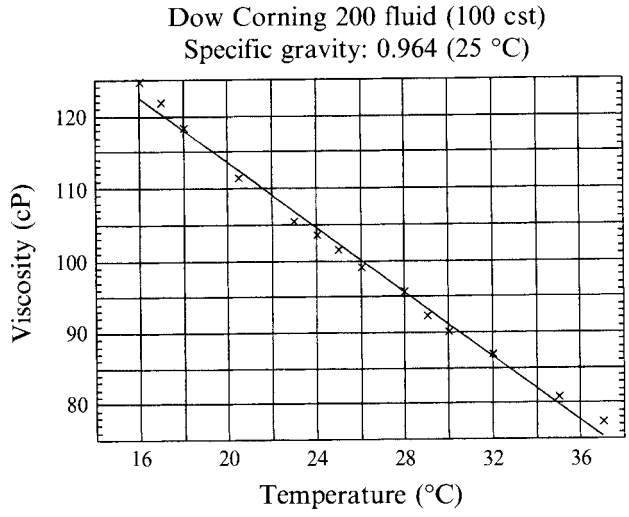

FIGURE 17. Viscosity *vs.* temperature of Dow Corning 200 fluid, specific gravity 0.964 at 25 °C (measured by Brookfield viscometer model DV-I).

Evaluate the first-order spatial derivatives on boundaries by the second-order forward or backward difference, i.e.

$$(x_\xi)_{1,j} = \frac{-3x_{1,j}+4x_{2,j}-x_{3,j}}{2\Delta\xi}, \quad (x_\eta)_{i,n} = \frac{3x_{i,n}-4x_{i,n-1}+x_{i,n-2}}{2\Delta\eta}.$$

It can be shown that the compatibility condition (B 1) is satisfied identically by summing (discrete form of integration) the above discretized terms:

$$\sum_{i=2}^{m-1}\sum_{j=2}^{n-1} \mathrm{LHS}(2.10a) - \sum_{j=2}^{n-1}\frac{1}{\Delta\xi}(\mathrm{LHS}(2.10b)\,|_{\xi=m} - \mathrm{LHS}(2.10b)\,|_{x=1}) - \sum_{i=2}^{m-1}\frac{1}{\Delta\eta}(\mathrm{LHS}(2.10c)\,|_{\eta=n} - \mathrm{LHS}(2.10c)\,|_{\eta=1}) = 0,$$

and

$$\begin{aligned}\sum_{i=2}^{m-1}\sum_{j=2}^{n-1} \mathrm{RHS}(2.10a) &- \sum_{j=2}^{n-1}\frac{1}{\Delta\xi}(\mathrm{RHS}(2.10b)\,|_{\xi=m} - \mathrm{RHS}(2.10b)\,|_{\xi=1}) \\ &- \sum_{i=2}^{m-1}\frac{1}{\Delta\eta}(\mathrm{RHS}(2.10c)\,|_{\eta=n} - \mathrm{RHS}(2.10c)\,|_{\eta=1}) \\ &= \left(\frac{0.5}{\Delta\xi}\right)\sum_{j=2}^{n-1}\left[\left(-\frac{1}{Re}\omega_\eta + x_\eta\frac{1}{Fd}\right)_{1,j} + \left(-\frac{1}{Re}\omega_\eta + x_\eta\frac{1}{Fd}\right)_{2,j}\right. \\ &\quad \left. -\left(-\frac{1}{Re}\omega_\eta + x_\eta\frac{1}{Fd}\right)_{m,j} + \left(-\frac{1}{Re}\omega_\eta + x_\eta\frac{1}{Fd}\right)_{m-1,j}\right] \\ &\quad + \left(\frac{0.5}{\Delta\eta}\right)\sum_{i=2}^{m-1}\left[\left(\frac{1}{Re}\omega_\xi - x_\xi\frac{1}{Fd}\right\}_{i,1} + \left(\frac{1}{Re}\omega_\xi - x_\xi\frac{1}{Fd}\right\}_{i,2}\right. \\ &\quad \left. -\left(\frac{1}{Re}\omega_\xi - x_\xi\frac{1}{Fd}\right\}_{i,n} + \left(\frac{1}{Re}\omega_\xi - x_\xi\frac{1}{Fd}\right\}_{i,n-1}\right] = 0.\end{aligned}$$

A similar operation can be done on multiply-connected regions with minor modifications.

Appendix C. Viscosity *vs.* temperature of Dow Corning 200 fluid

Figure 17 shows how the viscosity of the fluid used in the experiments varied with temperature.

REFERENCES

ABDALLAH, S. 1987 Numerical solutions for pressure Poisson equation with Neumann boundary conditions using a non-staggered grid, I and II. *J. Comput. Phys.* **70**, 182–202.

BIRINGEN, S. & COOK, C. 1988 On pressure boundary conditions for the incompressible Navier–Stokes equations using non-staggered grids. *Numer. Heat Transfer.* **13**, 241–252.

CASULLI, V. 1986 Eulerian–Lagrangian method for hyperbolic and convection dominated parabolic problem. In *Computational Methods for Nonlinear Problems*, pp. 239–269. Swansea: Pineridge.

CASULLI, V. 1987 Numerical solution of the Navier–Stokes equations at high Reynolds number. In *Numerical Methods in Laminar and Turbulent Flow*, vol. 5, Part 1, pp. 143–176. *Proc. Fifth Intl Conf., Montreal, Canada.*

CHANDRASEKHAR, S., 1981 *Hydrodynamic and Hydromagnetic Stability*. Dover.

COYLE, D. J. 1984 The fluid mechanics of roll coating: steady state flows, stability, and rheology. PhD thesis, University of Minnesota, Minneapolis.

DIPRIMA, R. C. & SWINNEY, H. L. 1981 Instabilities and transition in flow between concentric rotating cylinders. In *Hydrodynamic Instabilities and Transition to Turbulence*, 2nd edn. (ed. H. L. Swinney & J. P. Gollub) pp. 139–180. Topics in Applied Physics, Vol. 45, Springer.

GHIA, K. N., HANKEY, W. L. & HODGE, J. K. 1977 Study of incompressible Navier–Stokes in primitive variables using implicit numerical technique. *AIAA Paper* 77–648.

HACKBUSCH, W. & TROGGENBERG, U. (ed.) 1982 *Multigrid Methods*, Lecture Notes in Mathematics, vol. 960. Springer.

HIRT, C. W. & HARLOW, F. H. 1967 A general corrective procedure for the numerical solution of initial-value problems. *J. Comput. Phys.* 2, 114–119.

MANSOUR, M. L. & HAMED, A. 1990 Implicit solution of the incompressible Navier–Stokes equations on a non-staggered grid. *J. Comput. Phys.* **86**, 147–167.

MATISSE, P. & GORMAN, M. 1984 Neutrally buoyant anisotropic particles for flow visualization. *Phys. Fluids* **27**, 759–760.

RUSCHAK, K. J. 1981 A three dimensional linear stability analysis for two dimensional free boundary flows by the finite element method. *Comp. Fluids* **11**, 391–401.

SPARROW, E. M., MUNRO, W. D. & JONSSON, V. K. 1964 Instability of the flow between rotating cylinders: the wide-gap problem. *J. Fluid Mech.* **20**, 35–46.

TAYLOR, G. I. 1923 Stability of viscous liquid contained between two rotating cylinders, *Phil. Trans. R. Soc. Lond.* A **223**, 289–343.

THOMPSON, J. F., WARSI, Z. U. A. & MASTIN, C. W. 1982 Boundary-fitted coordinate system for partial differential equations – a review. *J. Comput. Phys.* **47**, 1–108.

THOMPSON, J. F., WARSI, Z. U. A. & MASTIN, C. W. 1985 *Numerical Grid Generation/Foundations and Application.* North-Holland.

WALOWIT, J., TSAO, S. & DIPRIMA, R. C. 1964 Stability of flow between arbitrarily spaced concentric cylindrical surfaces including the effect of a radial temperature gradient. *Trans. ASME.* E: *J. Appl. Mech.* **31**, 585–593.

WANG, F. J. 1990 Numerical simulation of free surface flows. PhD dissertation, Columbia University.